Comparative 3D ultrastructure of *Plasmodium falciparum* gametocytes

Felix Evers[1], Rona Roverts[2,3], Cas Boshoven[1], Mariska Kea-te Lindert[2,3], Robert E. Sinden[4], Anat Akiva[2,3], Taco W.A. Kooij[1*]

[1]Department of Medical Microbiology, Radboudumc Center for Infectious Diseases, Radboud University Medical Center, Nijmegen, The Netherlands.
[2]Electron Microscopy Center, RTC Microscopy, Radboud University Medical Center, Nijmegen, the Netherlands.
[3]Department of Medical Biosciences, Radboud University Medical Center, Nijmegen, the Netherlands.
[4]Department of Life Sciences, Imperial College London, London, UK.

* taco.kooij@radboudumc.nl

Abstract

Despite the enormous significance of malaria parasites for global health, some basic features of their ultrastructure remain obscure. In this study, we apply high-resolution volumetric electron microscopy to examine and compare the ultrastructure of *Plasmodium falciparum* gametocytes of both genders and in different stages of development as well as the more intensively studied asexual blood stages revisiting previously described phenomena in 3D. In doing so, we challenge the widely accepted notion of a single mitochondrion by demonstrating the presence of multiple mitochondria in gametocytes. We also provide evidence for a gametocyte-specific cytostome variant. Furthermore, we generate, among other organelles, the first 3D reconstructions of endoplasmic reticulum (ER), Golgi apparatus, and extraparasitic structures in gametocytes. Assessing interconnectivity between organelles, we find frequent structural appositions between the nucleus, mitochondria, and apicoplast. We provide evidence that the ER is a promiscuous interactor with numerous organelles and the trilaminar membrane of the gametocyte. Public availability of these volumetric electron microscopy resources of wild-type asexual and sexual blood-stage malaria parasites will facilitate reinterrogation of this global dataset with different research questions and expertise. Taken together, we reconstruct the 3D ultrastructure of *P. falciparum* gametocytes in high detail and shed light on the unique organellar biology of these deadly parasites.

Introduction

Parasites from the genus *Plasmodium* are the causative agents of malaria. This mosquito-borne infectious disease remains a huge burden on global public health with more than 200 million cases and >600 thousand fatalities in 2021 alone[1, 2]. Humanity's efforts to combat this disease have shown impressive results during the years 2000 – 2015 but have since stalled. This is largely driven by continuing emergence of resistance to all frontline antimalarials[3] as well as the inability of most antimalarials to combat directly the asymptomatic but transmissible sexual stages[4]. To stop parasite transmission and eliminate malaria, there is an urgent need for drugs with novel mechanisms of action, particularly those that are effective against sexual stages. The apicomplexan phylum, among which are the malaria parasites, diverged very early in eukaryotic evolution and some basic cellular processes and structures are comparatively poorly understood despite their immense significance for global health. In particular, *Plasmodium* organelle biology has been shown to deviate from standard eukaryotic models and varies drastically between the different life-cycle stages. Furthermore, Apicomplexa are almost exclusively parasitic, which drives additional divergence in cellular features related to their survival strategy, such as feeding, locomotion, secretion, invasion, and adaptation to their respective hosts. As a result, we are in the situation where there is urgency to find drug or vaccine candidates for cellular systems that are relatively poorly understood. In the case of *Plasmodium*, this holds particularly true for life-cycle stages, like the sexual gametocyte stages, that are less accessible than the pathogenic asexual blood-stage parasites (ABS).

Classical electron microscopy studies in the period from 1965-2000 provided key insights into the ultrastructure of malaria parasites and laid the groundwork for much of our understanding of sexual-stage biology[5-8]. There have been a few noteworthy serial sectioning electron microscopy (ssEM) applications[9-12], however, these early studies lacked the advanced quantitative, volumetric, and computational methods available today and did not have the context of our current molecular understanding of malaria parasite biology. With the advent of novel and, more importantly, increasingly accessible high-resolution volumetric approaches such as focused ion beam milling - scanning electron microscopy (FIB-SEM), serial block-face scanning electron microscopy (SBF-SEM), array tomography (AT), and expansion microscopy (ExM), we have made great advances in recent years. Features of ABS and oocysts and their respective replication strategies have been investigated via FIB-SEM with great success[13, 14]. ssEM and AT have recently been applied to elucidate the reputed role of nuclear microtubules in driving the characteristic elongation of developing gametocytes[15] and general measurements of gametocytes and insights underpinning the inner membrane complex (IMC) have been gained using SBF-SEM[16]. ExM has been used to elucidate microtubule dynamics across gametocyte development and during activation, and immunofluorescence-based studies have demonstrated that the mitochondrion dramatically branches and enlarges in the gametocyte stages[17-19]. Additionally, electron micrographs have shown that in contrast to the acristate mitochondrion in ABS, the gametocyte mitochondrion is highly cristate[6, 20, 21]. Yet, other organelles, such as the endoplasmic reticulum (ER), the Golgi apparatus (Golgi), and the cytostome, and their interconnectivity have not been subject to specific microscopic investigations in gametocytes and our general understanding of their morphology and putative interactions is largely derived from model eukaryotes or extrapolated from *Plasmodium* ABS.

In this study, we investigate the ultrastructure of gametocytes using high resolution FIB-SEM and ssSEM volumetric imaging. We compare our ultrastructural gametocyte findings with our ABS data and other

high-resolution volumetric studies. In doing so, we find evidence for a morphologically distinct cytostome in gametocytes, multiple mitochondria per cell, indications for widespread inter-organelle interactions, generate high-resolution renderings of various organelles and visualize 3D morphology and distribution of external structures in gametocytes. Additionally, we aim to create a reusable image resource for the malaria research community to investigate more cells from the FIB-SEM and ss-SEM data, contrast their own findings with a reference point, and reinterrogate the datasets with their specific biological question, perspective, and expertise.

Results and Discussion

General morphology of the gametocyte

The mature gametocytes show their typical crescent shape that is well known from light microscopy-based imaging (Fig. 1A, B). The surrounding red blood cell (RBC) also conformed to this general shape, with the Laveran's bib, a narrow ridge spanning between the tips of the parasite crescent, being evident in all stage IV and V gametocytes (Fig. 2). We also identified contorted mature gametocytes with a knicked appearance including a narrowing of the cytoplasm, a frequent aberrant morphology known from Giemsa preparations of gametocyte cultures (Supp. Fig. 1). We were surprised to find that aside from the deviating morphology, no other signs of poor health or differences of internal structures could be recognized in these contorted gametocytes. Immature gametocyte stages (stage II-IV) were identified based on their well-characterized straighter or more compact appearance and incomplete inner membrane complex (Supp. Fig. 2). With increased maturity, the overall electron density of the RBC cytoplasm decreases and an electron lucent corona surrounding the gametocyte becomes apparent, indicative of hemoglobin depletion (Supp Fig. 3). While we were unable to confidently assign sexes to earlier stages, we relied on differing patterns of hemozoin distribution together with the frequency and appearance of osmiophilic bodies (OBs) to differentiate male and female stage IV/V gametocytes. Whereas previously cytoplasmic density of ribosomes[22] was widely used to discriminate genders, we could not detect such differences in our preparations. OBs are vesicles that are abundant in females and thought to play a role during gametocyte egress from the RBC. *P. falciparum* males have been suggested to contain fewer OBs or even lack them completely[5, 23]. Our data show that *P. falciparum* males, contain vesicles that share morphological characteristics with OBs (Fig. 1B, Supp. Fig. 4A). As in *Plasmodium berghei*, these structures are much fewer in number in males than in females[24]. Furthermore, all or almost all OBs in male gametocytes have a "tail" that occasionally interconnects the vesicles - which is found only in a small subset of OBs in females (Supp. Fig. 4A, B). This tail has been observed previously in a thin section of a female *Plasmodium cathemerium* gametocyte and a *Plasmodium gallinaceum* gametocyte[25] but is largely absent from previous microscopic data of *P. falciparum* gametocytes. It would be interesting to investigate further whether these different observations reflect differences in underlying biology of the analysed parasites or methodological differences. One possible explanation is that paucity of prior observations might stem from a higher likelihood of identification in high-resolution volumetric data as opposed to individual thin slices or differing staining procedures that make these structures visible. In the rodent malaria parasite, *P. berghei,* male osmiophilic bodies have been shown to have a distinct but overlapping proteome compared to OBs identified in female gametocytes[24]. However, no morphological differences were evident from the presented representative micrographs. We hypothesize that the putative OBs identified in male *P. falciparum* gametocytes also differ in protein composition as males do not stain positive for the Pfg377 protein that readily stains OBs of female gametocytes[23]. Supporting this hypothesis a recent preprint suggests presence of two proteomically and

121 functionally distinct subtypes of vesicles that aid in gametocyte egress, one of which – in line with our
122 data - does not show any evidence for gender specificity[26].

123 To compare our gametocyte reconstructions with the more extenstively studied ABS[13], we reconstructed
124 two representative cells: a developing schizont that is still undergoing nuclear division and a fully
125 segmented schizont, (Fig. 1C, D). Overall 3D morphology and appearance of the structures in individual
126 slices match those observed by Rudlaff et al.[13] (publicly available from EMPIAR, entry 10392). The
127 developing schizont contains ten distinct nuclei and extensive mitochondrial and apicoplast networks
128 that permeate the whole cell. The segmenter is comprised of 31 fully formed daughter merozoites, each
129 containing mitochondrion, apicoplast, rhoptry pair, ER, micronemes, and nucleus, and an additional
130 (32nd) merozoite that lacks a nucleus. Even at this late stage of development, without exception, each
131 merozoite is still connected to the residual body that surrounds the food vacuole (Fig. 1C). This
132 connectivity is highlighted by one merozoite that is connected to the residual body through an
133 elongated neck/tube (Supp. Fig. 5A). Furthermore, the residual body is connected to the RBC cytoplasm
134 via two continuous tubes, presumably facilitating continued sustenance to the daughter merozoites
135 until rupture. Our data also contain occasional extracellular merozoites, most likely due to schizonts
136 rupturing in the interval between magnetic separation and fixation. Comparing released extracellular to
137 the intraerythrocytic merozoites, we find that volumes of the overall merozoite and individual
138 organelles are very similar, supporting the notion that the corresponding segmented schizont is close to
139 full maturity (Fig. 1D). The only dimension on which the extracellular and intracellular merozoites differ
140 is that the extracellular merozoite is spherical while the average intracellular merozoite conforms to a
141 tooth-like shape, likely due to space constraints in the schizont and to maintain a connection to the
142 residual body throughout development. This observation is consistent with data from *Plasmodium*
143 *knowlesi* and a post PVM-rupture *P. falciparum* schizont[13, 27]. Other characteristics of the ABS are
144 described in comparison with the gametocyte in other sections below.

145

146

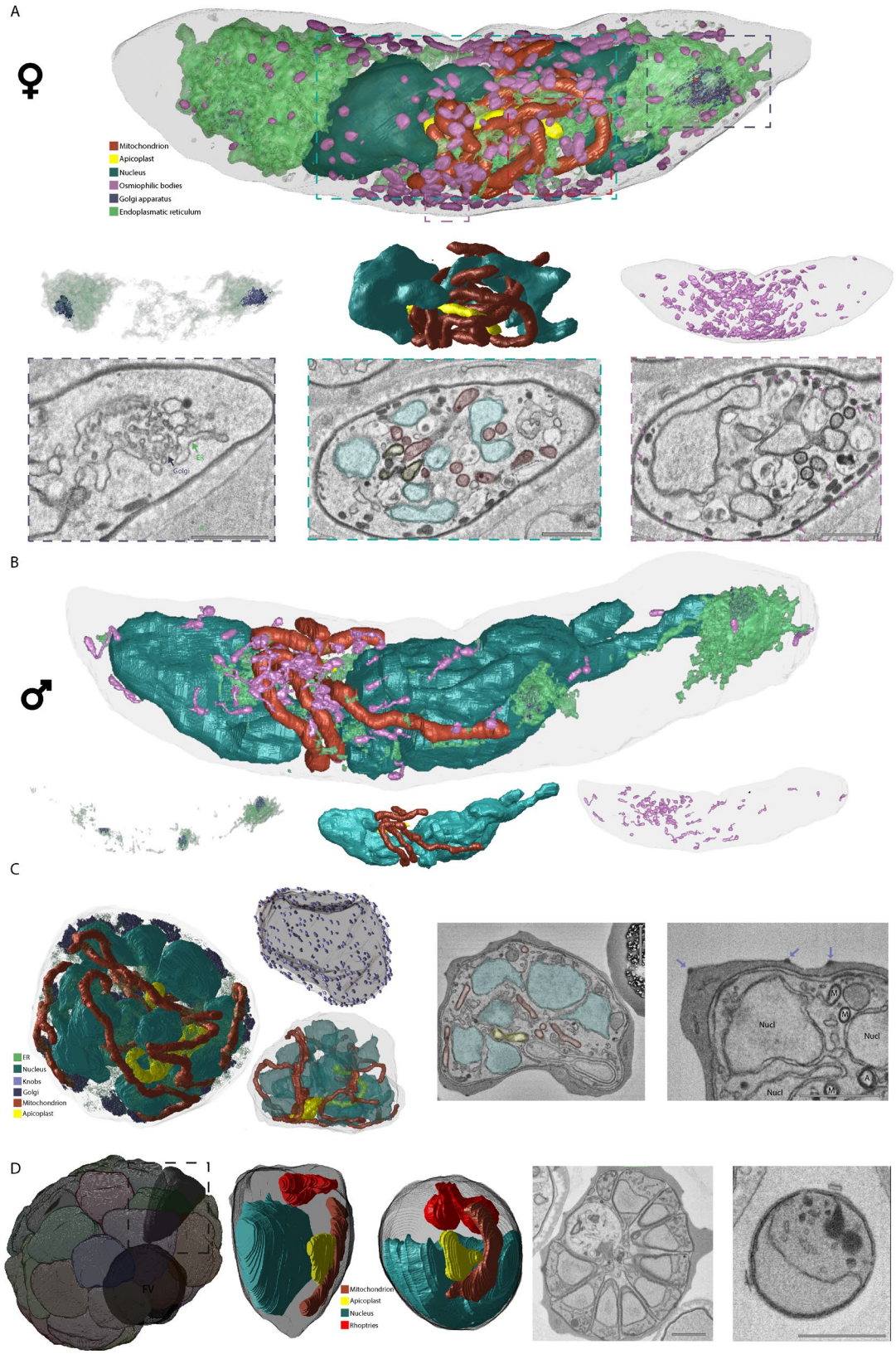

Figure 1 | **Ultrastructural features and renderings of mature gametocytes, early schizont and segmented schizont**
A Rendering of ultrastructural features of a mature female gametocyte and specific renderings of Golgi apparatus and ER distribution (left panel), relation of nucleus/apicoplast/mitochondrion (middle panel) as well as distribution and appearance of osmiophilic bodies. Appearance of rendered structures in exemplary micrographs is matched to rendered features through color-coded dashed lines. Scale bar = 1 µm **B** Rendering of ultrastructural features of a mature male gametocyte and specific renderings as in (A). Note the relative paucity of ER, Golgi and osmiophilic bodies relative to the female gametocyte. The

osmiophilic bodies differ morphologically with overall thinner appearance and frequent tail-like extensions. **C** Rendering of ultrastructural features of an early schizont and specific rendering of relation of nucleus/apicoplast/mitochondrion as well as individual knob distribution. Appearance of ultrastructural features is shown in two exemplary micrographs. Scale bar = 1 µm M = Mitochondrion; ER = Endoplasmic reticulum; Nucl = Nucleus; FV = Food vacuole **D** Rendering of daughter merozoites within a segmented schizont and rendering of one intracellular and one extracellular merozoite with ultrastructural features. Overview on appearance of the two merozoite shapes is shown in two exemplary micrographs. Scale bar = 1 µm

Parasite-induced modifications of the red blood cell

RBCs infected with mature gametocytes contain flat, membranous disks (Fig. 2A, B) that differ from the characteristic membranous stacks called Maurer's clefts we observed in ABS-infected RBCs (Fig. 2C). In gametocytes of both genders, extraparasitic structures were less frequent, generally larger but heterogenous in size and unevenly distributed within the RBC cytoplasm (Fig. 2A, B). We consistently find a higher density of extraparasitic structures in the Laveran's bib that spans between the two ends of the mature gametocyte[28]. This matches results of previous work that found accumulation of a class of exported proteins to this subcellular location[29]. Furthermore, we find an occurrence of a 'Garnham body', a rare gametocyte exclusive structure originally discovered in 1933 with still unknown functional significance[30] (Supp. Fig. 6). Our data confirm the highly membranous appearance of the Garnham body described in previous micrographs and specifically we identify four double membranes . However, we found no associated hemozoin, which was identified in some light microscopy examples[5, 6, 22, 31] (Supp. Fig. 6A, B). The Garnham body was found adjacent to but not within the Laveran's bib, at a site devoid of IMC and situated in the vicinity of the opening of the cytostome (Supp. Fig. 6C). The presence of a Garnham body in the RBC also coincides with electron dense protrusions of the parasite vacuolar membrane radiating in all direction from the parasite and a membranous electron lucent compartment within the parasite, that were observed in no other cells (Supp. Fig. 6A, B). These concurrent exclusive features could indicate Garnham bodies to be a sign of an unhealthy gametocyte and/or RBC or suggestive of a rare subtype in gametocyte populations.

Consistent with published literature, the plasma membrane of gametocyte-infected RBCs is not visibly modified, while the ABS-infected cells are thoroughly covered by uniformly distributed knobs, which are proteinaceous parasite-derived protrusions that mediate cytoadherence of ABS-infected RBCs[32] (Fig. 1C). Reconstructions suggest a total of 390 knobs on the surface of the early schizonts-infected RBC corresponding to 2.9 knobs/μm^2 (Fig. 1C), which is in line with previous measurements obtained for NF54-infected RBCs via atomic force microscopy[33]. The overall surface profile of the segmenter-infected RBC appeared more uneven with more peaks and valleys compared to the developing schizont, while gametocyte-infected RBCs appeared to have a smoother surface profile than either (Supp. Fig. 5B, C, D). As anticipated, the trilaminar membrane architecture of the gametocyte-RBC interface, consisting of the parasite vacuolar membrane (PVM), the parasite plasma membrane (PM) and the IMC, is evident from the micrographs. Localized areas of further thickened IMC membrane might represent the leading edge of IMC plates[16] while areas without IMC cover in immature stages suggest ongoing IMC plate biogenesis (Supp. Fig. 7 A, B). In mature stages, we occasionally find similar IMC overhangs of unknown significance (Supp. Fig. 7C).

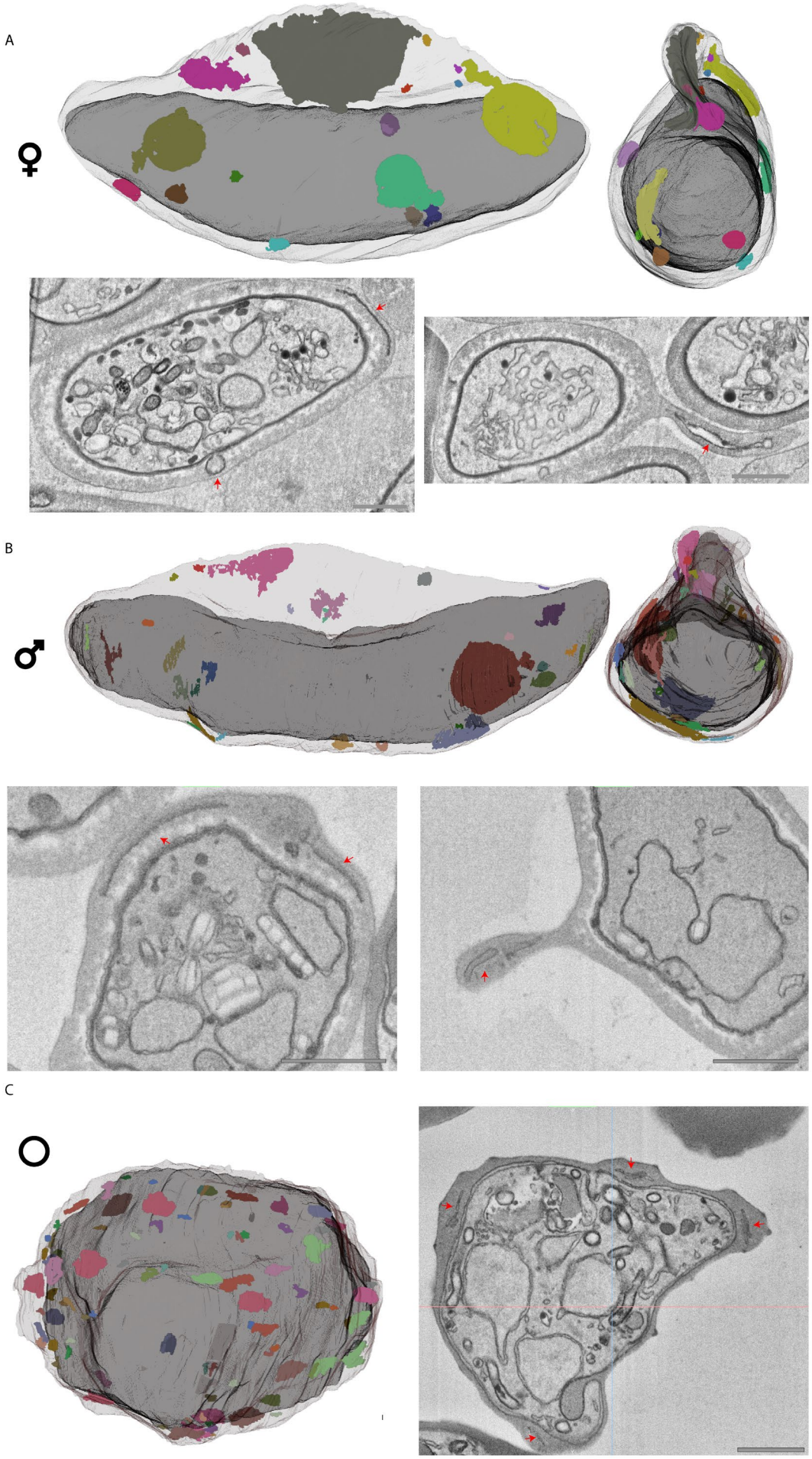
A
♀
B
♂
C

194 *Figure 2* | **Extraparasitic structures differ in gametocytes and ABS**
195 Mature female (**A**), male (**B**) gametocyte and early schizont (**C**) rendered with RBC outline and extraparasitic structures in
196 different color for each membrane structure. Gametocyte renderings are shown from two angles. Examples of extraparasitic
197 structures in micrographs are highlighted with red arrows. Scale bar = 1 µm.

198

199 **The gametocyte cytostome**

200 RBC-parasite interactions are not restricted to host-cell modification, but also include the internalization
201 and digestion of host-cell cytoplasm to fuel parasite growth. An unusual feeder organelle, the cytostome
202 (meaning cell mouth), facilitates this uptake of RBC cytoplasm in ABS[12]. In our micrographs of ABS and
203 other studies[34], the cytostome presents itself as a hemoglobin filled tube surrounded by a double-
204 membrane and possessing an electron dense "neck", called the cytostomal collar, at the invagination
205 site (Supp. Fig. 8). Gametocytes similarly rely on hemoglobin internalization and digestion. Putative
206 morphologically diverse cytostomes have been assigned in past EM studies[5, 6]. When trying to assign the
207 cytostome in mature gametocytes, we came across likely yet distinct candidate structures. Presenting a
208 clear invagination of the parasite membranes, the structures are always surrounded by extensive ER but
209 otherwise can be subdivided into three categories (Fig. 3A). In 44% of the evaluated examples (n = 50),
210 the organelle has a membrane delimited electron dense ring that is 100-160nm thick and connected to
211 the RBC cytoplasm while the lumen circumscribed by the ring appears electron lucent and can
212 occasionally contain further membranous or dark stained structures. In 40% of the cases the structures
213 had a more ABS-like appearance with no clear delineation into ring and lumen but circular grooves on
214 the inside of the membrane that are absent in the ABS cytostome potentially indicative of future
215 emergence of the ring structure. In the remainder the ring is relatively larger with inconsistent thickness
216 and a smaller electron lucent internal lumen potentially representing an in-between state. Furthermore,
217 it appears that each gametocyte that we have fully imaged only contains a single cytostome of any of
218 these three gametocyte-specific subtypes. Conversely, in ABS multiple cytostomes have been reported[35]
219 and are also evident from our data with a maximum of seven cytostomes per cell (Supp. Fig. 8, panel 3).
220 Interestingly, in one example of a developing gametocyte, we find both a canonical ABS-type cytostome
221 and a gametocyte variant (Fig. 3B). This observation suggests that the structure we identified in
222 gametocytes might be entirely distinct from the cytostome. In mature stages, hemoglobin
223 internalization is largely finished and consequently the cytostome may no longer be required for its
224 canonical purpose. It is tempting to speculate that this cytostome variant is instead involved in host lipid
225 acquisition, as parasite lipid content dramatically increases throughout gametocytogenesis[36]. This would
226 also offer a plausible explanation for the ER, as the primary site of lipid metabolism, consistently
227 surrounding the cytostome and would suggest that the occasional dark contents of the lumen seen in
228 our preparations are (osmiophilic) lipids.

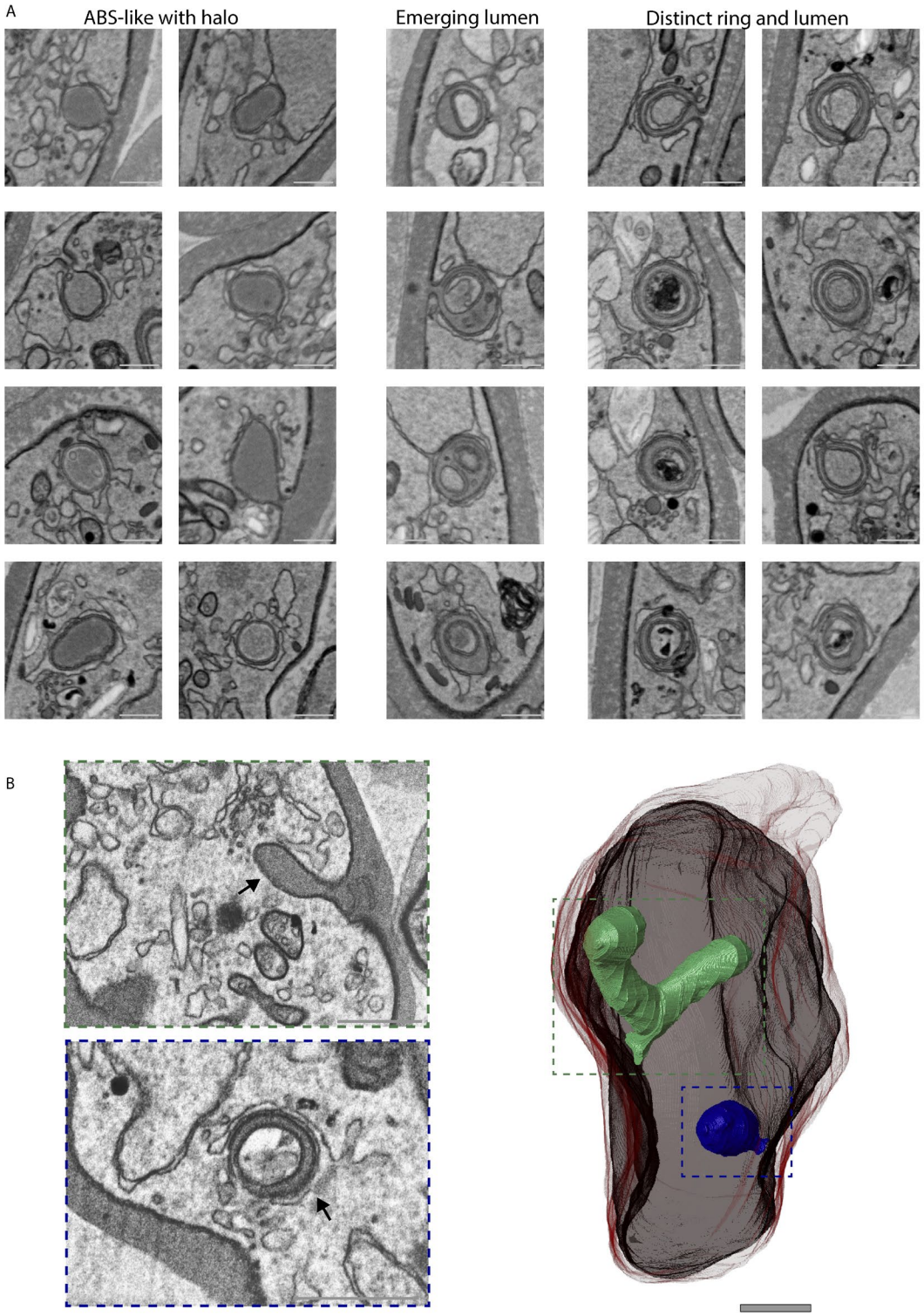

229

230 *Figure 3* | **The gametocyte cytostome**
231 **A** Exemplary micrographs of the cytostome in 20 different gametocytes subidivided into three categories. **Left**: Cytostome
232 without further membrane delineation in lumen, relatively homogenous lumen and circular grooves that could indicate future
233 emergence of ring **Middle**: Relatively large membrane electron dense ring and small electron lucent lumen. Ring is continuous
234 with RBC cytosol, putative intermediate state **Right**: Electron dense ring with homogenous thickness and lumen with
235 heterogenous content. Ring is continuos with RBC cytosol. All categories have close association of ER unlike the ABS cytostome.
236 Scale bar = 0.1 µm **B** Rendering of a developing gametocyte that contains both a canonical ABS cytostome and a cytostome with
237 distinct ring and lumen. The ABS cytostome (green) is characterized by homogenous dark lumen and continuation of the

238 parasite membrane that forms the invagination. The gametocyte cytostome (blue) is characterized by a bulbous shape and
239 distinct electron dense ring with electron lucent lumen.

240 **The gametocyte ER and Golgi-apparatus**

241 Universally the ER is an extensive interconnected organelle continuous with the nuclear envelope that
242 serves as a transport hub, hosts various critical cellular functions, is widely connected with other
243 organelles, and even acts as a mediator of organellar interactions[37]. We find that the ER in both
244 developing gametocytes and mature female gametocytes is extensive and occupies large parts of the
245 cell, similar to the early schizont (Fig. 1A, Supp. Fig. 1, Supp. Fig. 2). The mature male gametocyte on the
246 other hand appears to contain much less ER, which is in line with previous observations and proteomic
247 data[38, 39] (Fig. 1B). It is noteworthy that in the mature female gametocyte, the ER is most dense in the
248 polar regions of the parasite. This coincides with the distribution of a closely associated organelle, the
249 Golgi, which, in *Plasmodium*, takes the rudimentary form of dispersed unstacked cisternae and is
250 recognizable as a smooth membraned vesicle cluster[22, 40-42]. In females, the Golgi is found in two distinct
251 clusters at both polar ends, while in the mature male it appears in four smaller clusters, similar to the
252 developing gametocytes that also have a more widespread distribution. Compared to the gametocytes,
253 the Golgi is much more extensive in the early schizont and found in evenly dispersed clusters around the
254 cell (Fig. 1C).

255 **The ER as a putative path across the IMC**

256 The ER also facilitates the extensive host-cell remodeling that occurs in ABS. In *P. falciparum*, an
257 estimated lower bound of 300 unique proteins, >5% of the proteome, is exported to the host cell to
258 modify aspects such as cytoadhesion, the host cytoskeleton, or nutrient permeability[43]. Proteins
259 destined for export are processed in the ER and delivered to the PM via vesicular transport and then
260 forwarded to the ***P**lasmodium* **T**ranslocon of **EX**ported proteins (PTEX) in the PVM, which translocates
261 the proteins into the host cell. While extensively researched in ABS, we know relatively little about how
262 this process translates to the gametocyte situation. Maurer's clefts appear absent in gametocytes,
263 possibly replaced by other cleft-like structures[44], and the gametocyte exportome is distinct from the ABS
264 exportome[45]. Whilst protein export machinery is essential for early gametocyte development[46, 47],
265 protein export has not been conclusively demonstrated in gametocytes beyond stage III. Indeed, as the
266 IMC cover increases, staining of the export machinery on the PVM becomes less pronounced or even
267 disappears completely in *P. falciparum* and *P. berghei* gametocytes, respectively[45, 48]. If protein export
268 still happens in late gametocyte stages the mechanism by which the additional barrier presented by the
269 IMC is overcome, is currently unknown[49]. In mature gametocytes, we frequently find sites at which the
270 ER runs very close to or is in direct contact with the parasite membrane (Supp. Fig. 9). From our
271 observations this interaction can manifest in a few different forms. The most frequent observation is
272 that ER directly contacts the IMC, leading to a continuity between these two compartments as well as
273 local disruption of the IMC (Supp. Fig. 9A) Less frequently but consistently we observe "budding" of a
274 piece of ER that contacts the parasite membrane (Supp. Fig. 9B). These local continuities between ER
275 and IMC might represent a mechanism to bridge the IMC and allow canonical ER-derived vesicle fusion
276 with the PM or facilitate alternative means of protein export. In developing gametocytes with
277 incomplete IMC cover we find that all extension sites are subject extensive ER interaction with the
278 nascent IMC (Supp. Fig. 9D) This is in line with previous EM-based observations that the outer nuclear
279 envelope interacts with nascent IMC and the PPM in developing gametocytes[15] and with
280 immunofluorescence microscopy data suggesting regions of ER contact with the IMC[50]. Even in mature

281 gametocytes with complete IMC cover we too find sites at which ER converts to electron dense material
282 that resembles IMC (Supp. Fig. 9C). Taken together, these observations, while anecdotal, provide further
283 evidence for a dynamic interplay between ER and IMC biogenesis or maintenance and suggest a
284 speculative mechanism to bridge the additional membrane layer in gametocytes for protein export.

285 **Features of *Plasmodium* mitochondria**

286 In gametocytes, the mitochondria are readily recognizable based on their cristate appearance and two-
287 layered membrane (Fig. 1). The cristae appear to have some degree of interconnectivity, consistent with
288 previous interpretations of tubular cristae, based on segmentations but the small size of the structures
289 and variability between slices, even at a z-resolution of 15nm, makes clear assertions of connectivity
290 challenging (Supplementary Movie. X). In appearance, the cristae are similar to the recently described
291 bulbous cristae in the related apicomplexan parasite *Toxoplasma gondii*[51]. In line with previous reports,
292 the mitochondrion is double-membraned yet acristate in ABS. In both ABS and gametocyte
293 mitochondria, we regularly identify electron dense mitochondrial granules (EDMGs) that appear in
294 clusters of 1-10 EDMGs and are heterogeneous in volume with a notably smaller size, propensity to be
295 more separate and more slender shape in ABS (Fig. 4A) [52, 53]. While they have not been described before,
296 they are readily recognizable in the image stacks of schizonts made public by Rudlaff *et al.*[13], indicating it
297 is not a unique feature of our preparations. The electron dense appearance could suggest that these
298 granules are sub-compartments that are either very proteinaceous or contain polysaccharides, lipids, or
299 mitochondrially relevant metals such zinc, calcium, copper, and/or iron. *P. falciparum* mitochondria
300 have been shown to play a role in calcium mobilization and storage[54] and so-called matrix granules that
301 are heavily enriched in calcium phosphate have been found in mammalian mitochondria[55]. In parasites
302 isolated from fish digestive tracts, similar mitochondrial granules have been shown to store glycogen,
303 which our staining procedure is particularly well suited to show[56, 57]. Increase of energy storing granules
304 in gametocyte stages could be a plausible preadaptation for survival in the relatively nutrient deprived
305 environment of the mosquito midgut. Alternatively, the EDMGs could represent the mitochondrial RNA
306 granules described in mammalian mitochondria. These are highly proteinaceous, non-membrane
307 delimited sub-compartments in the mitochondrial matrix that are thought to play an important role in
308 mitochondrial RNA processing, mitoribosome assembly, and gene expression[58]. As mitochondrial
309 translation in *Plasmodium* purely relates to complex III and complex IV components of the respiratory
310 chain, this could explain the discrepancy in EDMG size between the comparatively respiratory chain-
311 poor ABS compared to the respiratory chain-rich gametocytes[20, 59].

312

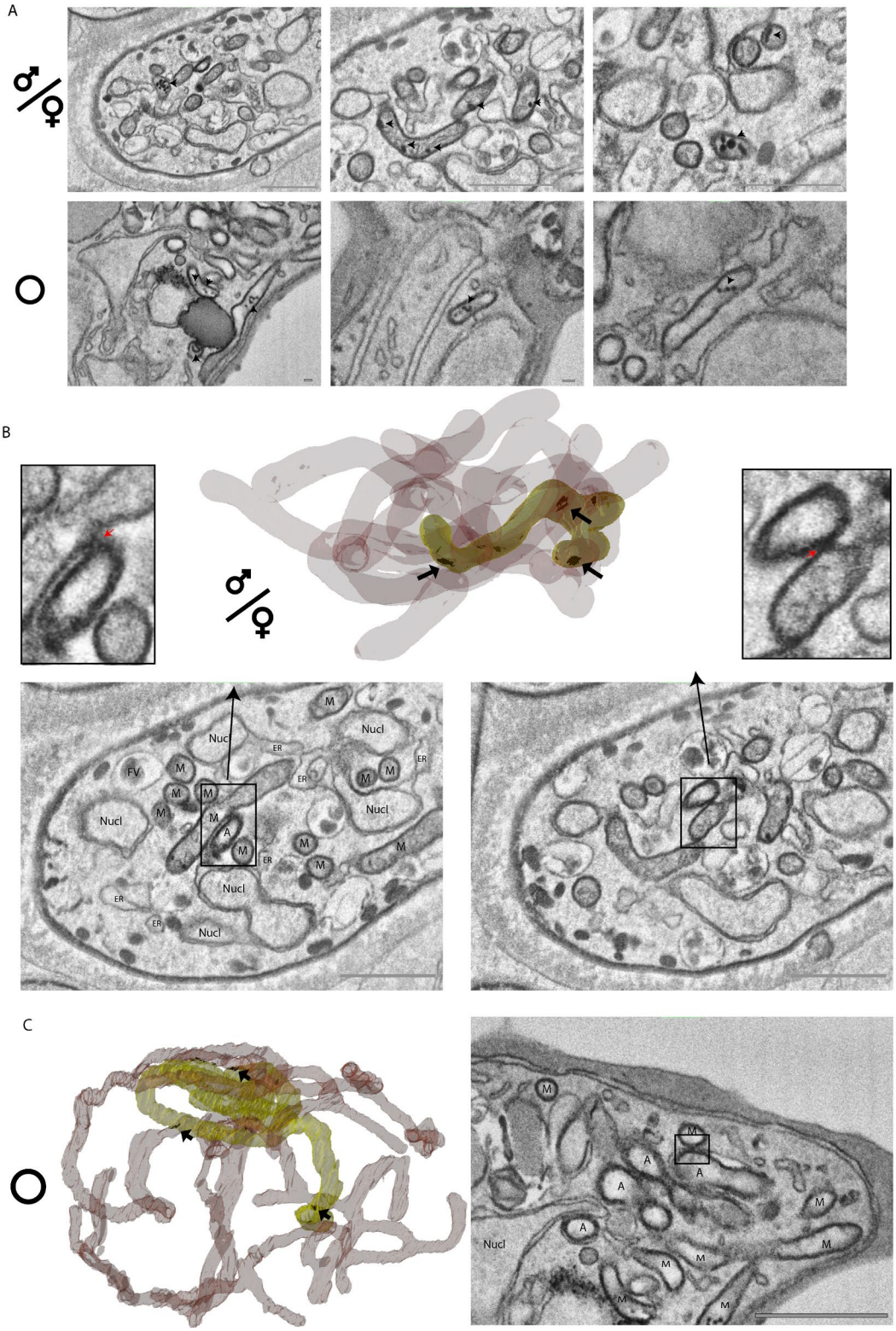

313

314 *Figure 4 |* ***Mitochondrial vesicles and interaction with the apicoplast***
315 ***A*** *Representative micrographs of EDMVs in gametocytes (upper panel, Scale bar = 1 µm) and asexual blood stages (lower panel,*
316 *Scale bar = 0.1 µm). Arrowheads highlight examples of EDMVs.* ***B*** *Rendering of exemplary gametocyte mitochondrion (red, high*
317 *transparency) and apicoplast (yellow, low transparency) with putative organelle interfaces rendered in black. Representative*
318 *micrographs for two interfaces and respective zoomed crops are shown below. Scale bars = 1 µm****C*** *Same representation as panel*
319 *above for an early schizont M = Mitochondrion; ER = Endoplasmic reticulum; Nucl = Nucleus; FV = Food vacuole*

320

321 **Multiple mitochondria in disguise**

322 The current consensus is that, like ABS, gametocytes contain a single heavily branched mitochondrion
323 with diverse morphology that does not closely correspond to gametocyte sex or maturity[19]. Hence, we
324 were surprised to find that while branched and clustered, we did not encounter a fully interconnected
325 mitochondrion in our imaged gametocytes. Instead, we found multiple mitochondria (5-10) per cell that,
326 while clustered and with close membrane appositions, did not share a continuous lumen. To investigate
327 this further, we carefully revisited mitochondrial morphology of a larger number of mature gametocytes
328 using fluorescence microscopy. As expected, most images gave the impression of a fully interconnected
329 organelle but we also found examples where at least some mitochondrial staining appeared separate
330 from the major cluster. This is consistent with the FIB-SEM data, where completely separated
331 mitochondria can be observed (Supp. Fig. 10 A), though in most cases the mitochondria are in close
332 proximity, potentially even suggestive of homotypic membrane interactions that are commonplace
333 among fungal and mammalian mitochondria[60] (Fig. 5B). These short distances of <50nm are well below
334 the diffraction limit of conventional fluorescence microscopy and would appear as a continuous
335 organelle. We observed no morphological indications for poor gametocyte health, which was confirmed
336 by normal gamete activation and the ability of male exflagellation. Moreover, exflagellating males have
337 clearly distinct, dispersed, and rounded mitochondria (Fig. 5D). In our FIB-SEM data, we identified one
338 comparable example of a male gametocyte showing bloated, rounded, and dispersed mitochondria that
339 appeared to be in the process of separating, though at this point it is unclear whether this is a male
340 gametocyte at the onset of activation or an aberrant cell (Supp. Fig. 10 B). We find occasional mature
341 male gametocytes showing a similar pattern using fluorescence microscopy (Supp. Fig. 10C). In
342 comparison, the asexual developing schizont possesses a single mitochondrion with a continuous lumen,
343 consistent with previous observations, suggesting that the observed phenotype is not directly caused by
344 fixation or sample processing (Fig. 1C)[13]. Taken together, we find consistent evidence for deviation from
345 the current consensus of a fully interconnected mitochondrion in gametocytes. Functional significance
346 of this deviation and appearance in other strains and culturing systems remain to be investigated.

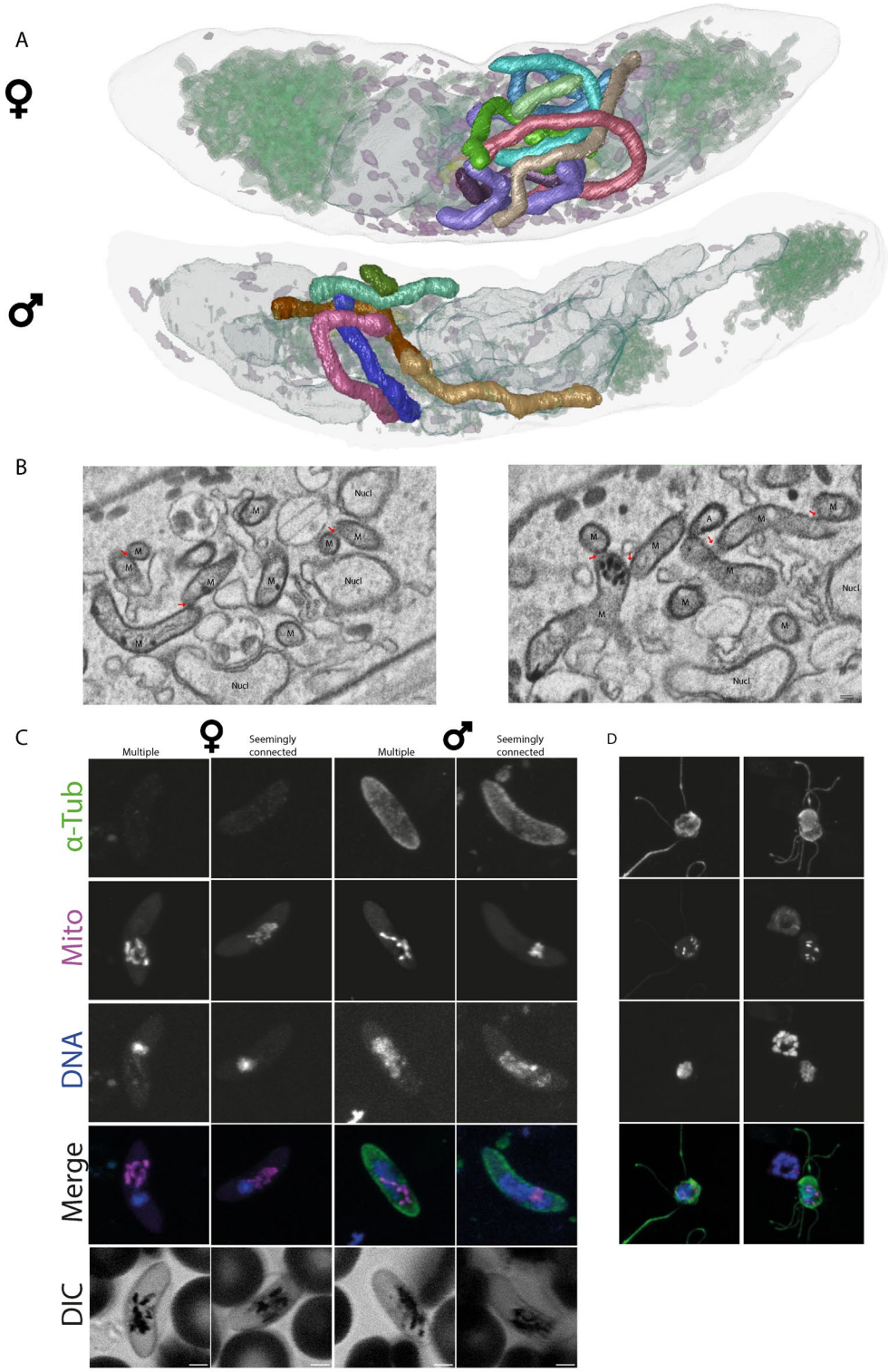

Figure 5 | **Gametocytes contain multiple mitochondria in close vicinity**
A Rendering of mature female (upper panel) and male gametocyte (lower panel). Each mitochondrion is rendered in a separate color. The male gametocyte has six distinct mitochondria while the female gametocyte has nine distinct mitochondria. In the female gametocyte membrane appositions are more frequent and mitochondria are more closely associated. Nucleus, osmiophilic bodies, ER, golgi and apicoplast are rendered with high transparency to provide cellular context. **B**. Exemplary micrographs showcasing membrane apposition between different mitochondria indicated by red arrows. The mitochondrial membrane remains intact at these sites and no continuity between the different mitochondria is evident. Scale bar = 0.1 µm M = Mitochondrion; A = Apicoplast; Nucl = Nucleus **C** Immunofluorescence analysis of mature and female gametocytes. Depicted left to right are maximum intensity projections using anti-α-tubulin antibodies, MitoTracker™ , DAPI, merge of all channels and

differential interference contrast (DIC) images. α-tubulin was used to distinguish male and female gametocytes, DNA was visualized using DAPI and mitochondria were visualized using MitoTracker. For each gender one example was given for recognizably separate mitochondria and a seemingly interconnected mitochondrion. Scale bar = 2 µm **D** Immunofluorescence analysis of exflagellating male gametes. Channels are the same as in **C.** Mitochondria are clearly separate and dispersed throughout the cell body.

Appositions of mitochondrion and apicoplast

In gametocytes, the mitochondria form a network that is wrapped around the apicoplast (Fig. 1 A, B, Supp. Fig. 1). The apicoplast is recognizable as a clearly distinct structure from the mitochondrion due to the thicker appearance of its four surrounding membranes and lack of internal membranous structures and more electron lucent lumen. The mitochondrial-apicoplast network is not spread throughout the whole cell but localized to a relatively central area of the gametocyte, always adjacent to the nucleus. It is noteworthy that this association and the mitochondrial network is much tighter than what we observe in early schizonts where the mitochondrion permeates the whole cell (Fig. 1C). The tight association is clearly distinct from the spatial separation of these organelles in sporozoites but akin to the tight association that has been observed in liver-stage parasites[61, 62]. Next to a general vicinity of the two organelles, we observe electron dense junctions spanning the membranes of the two organelles in both gametocyte and ABS (Fig. 4B, C). While it remains unresolved whether these sites constitute a true MCS (Information Box 1), the thickened electron dense interaction area is indicative of a tethering structure, providing a reasonable explanation why the organelles are consistently co-purified[63]. While a putative physical connection does not provide mechanistic evidence, the observed phenomenon may facilitate metabolic cooperation, *e.g.* by serving as an exchange site for metabolites of the heme biosynthesis pathway for which the enzymes are localized partly in the mitochondrion and partly in the apicoplast[64, 65].

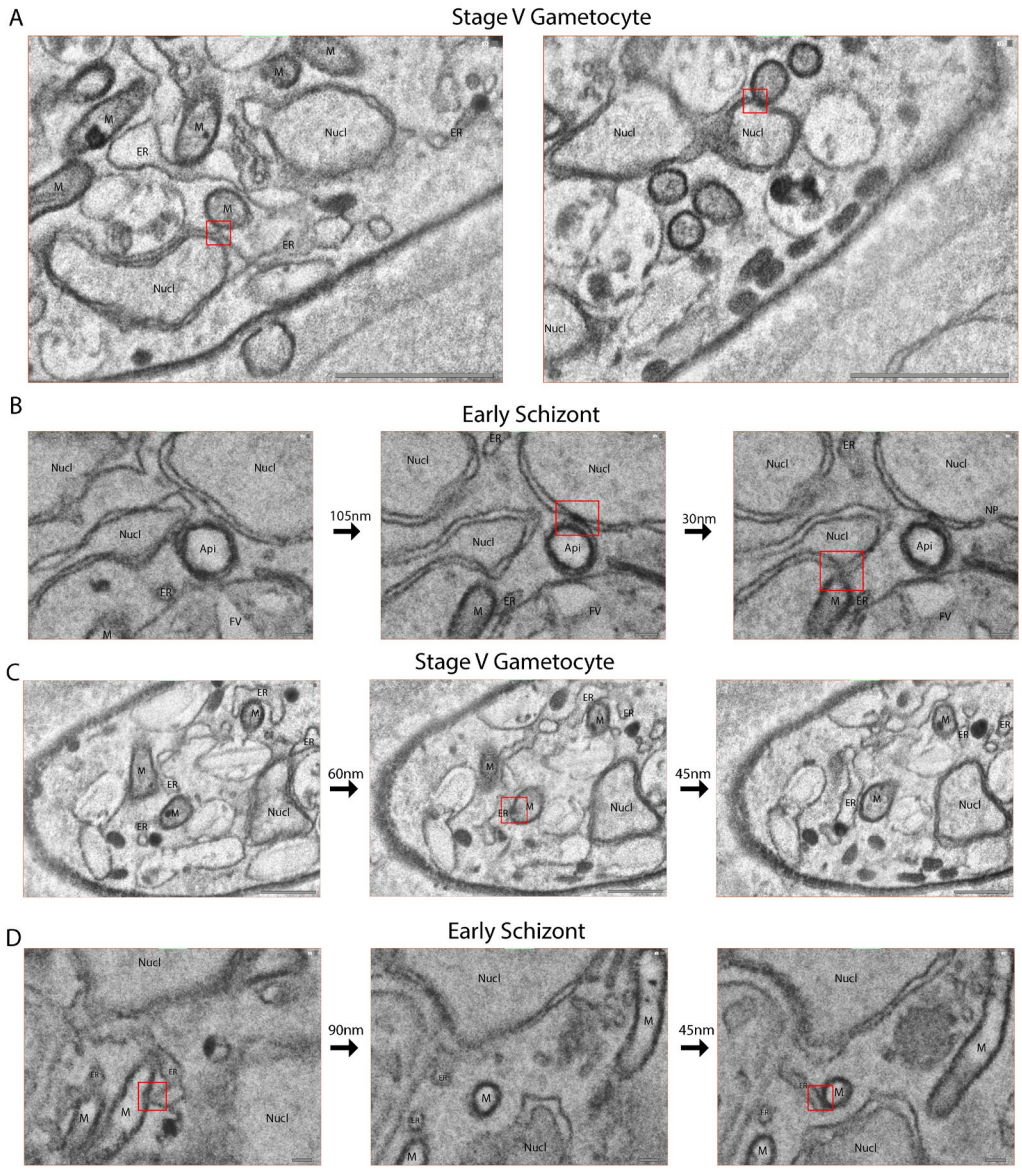

Figure 6 | **Putative organelle interfaces in blood stages**
A Representative micrographs showing putative mitochondrion-nucleus interaction sites in a mature gametocyte. The respective sites are highlighted through a red box. Scale bar = 1 µm **B** Representative series of micrographs showing putative mitochondrion-nucleus and apicoplast-nucleus interaction sites in an early schizont. The three frames are crops at the same x,y-coordinates in the acquisition plane but are at different z-depth with the respective distance displayed between micrographs **C** As in (B), showing putative mitochondrion-ER interaction sites in a mature gametocyte. Scale bar = 1 µm **D** As in (B), showing putative mitochondrion-ER interaction sites in an early schizont. Scale bar = 0.1 µm M = Mitochondrion; ER = Endoplasmic reticulum; Nucl = Nucleus; FV = Food vacuole

Appositions of ER and mitochondrion

From mammalian and yeast mitochondria, we know that the ER is intimately linked to and interacts with the mitochondrion through MCS. In these species, MCS cover 2-5% of the mitochondrial surface area and are composed of a known set of interactive proteins[66, 67]. These sites are thought to be crucial for lipid homeostasis and calcium transport. In our data, we similarly find multiple sites where the ER is in

396 very close proximity to the mitochondrion (Fig. 6C, D). Anecdotally, both in the early schizonts and
397 gametocytes, we find examples where these sites are accompanied by EDMGs appearing to span the
398 mitochondrial membrane and contact the ER (Supp. Fig. 11), which provides tentative support for a role
399 of EDMGs in calcium storage and/or mobilization. The appearance of the ER-mitochondrion appositions
400 resembles micrographs of previously described ER-mitochondrion MCS[68], leading us to believe that they
401 are conserved in *Plasmodium*. However, from all previously described tethering complexes, the
402 *Plasmodium* genome is lacking at least one critical component[69-72]. In *S. cerevisiae*, the ER membrane
403 complex (EMC) and TOM5 facilitate phospholipid exchange between ER and mitochondrion[73]. Recently,
404 we demonstrated that an assembled EMC is present in *P. falciparum*[20], but a TOM5 orthologue is not
405 encoded in *Plasmodium*. This prompted us to re-interrogate the underlying complexomics data and look
406 for another potential mitochondrial interactor with the EMC. In doing so, we found that *Pf*TOM7,
407 another component of the translocase of the outer membrane (TOM) complex, comigrates in native
408 electrophoresis with the EMC as well as the TOM complex (Supp. Fig. 12A). While overall structural
409 features of *Pf*TOM7 and *Sc*TOM7, based on alignment of the *Pf*TOM7 alphafold prediction[74] and
410 experimentally determined structure of *Sc*TOM7[75, 76] appear similar, *Sc*TOM5 is expectedly less similar
411 outside of the (predicted) TM helix (Supp. Fig. 12D). Looking at the multiple sequence alignment, few
412 residues are conserved outside of the transmembrane region and none are shared between *Sc*TOM5
413 and *Pf*TOM7 (Supp. Fig 12B). This suggests that if *Pf*TOM7, based on comigration with the EMC complex,
414 is a tether, the specific binding site is unlikely to be conserved. If a different mechanism tethers these
415 two complexes, it might also suggest that there is biological utility in specifically facilitating the tether
416 through a component of the TOM complex.

417 **Features and dimorphism of the gametocyte nucleus**

418 The nucleus is bounded by an inner and outer leaflet of the nuclear envelope, where the outer leaflet is
419 continuous with the ER and the inner leaflet circumscribes the nucleus. In gametocytes, we find an
420 intriguing deviation from the typically round or oval nuclear shape[77]. The nuclei share a bulbous body
421 from which thinner diverse extensions extrude predominantly in one direction covering large parts of
422 the cell (Fig. 7A, B). The bulbous body always contains a more electron dense, not membrane-bound
423 region, which has previously been assigned as the nucleolus of the female gametocyte[22] (Fig. 7C). The
424 observed nuclear shapes are largely consistent with prior studies that noted a discrepancy between a
425 relatively small and localized DNA stain and an elongated staining from a nucleus-targeted
426 fluorophore[15, 78]. In stage IV – V gametocytes, a clear nuclear dimorphism is apparent with female
427 gametocytes possessing a less complex smaller nucleus with an average volume of 6.6 ± 0.3 μm^3, while
428 males have a more complex nuclear shape and a much higher nuclear volume at 12.4 ± 1.1 μm^3(Fig. 7B).
429 A comparatively enlarged nucleus in males is consistent with well-known differences observed in
430 Giemsa-stained samples and might prepare male gametocytes for the rapid nuclear division and DNA
431 replication that they undergo upon activation. While smaller, the female nucleus is still relatively large,
432 possibly explained by the proposed role of the nuclear extension in elongation of the gametocyte[15].
433 Based on our measurements, for merozoites the same genetic material fits into a nucleus of ~0.5 μm^3
434 while for our exemplary early schizont in the process of DNA duplication, average nuclear volume is
435 around 1.8 μm^3. Stage II - III immature gametocytes also reflect the nuclear dimorphism observed in
436 stage IV – V gametocytes, with some having a relatively smaller and less complex nucleus while another
437 subset has a bigger and more complex nucleus (Fig. 7A). While we cannot confidently assign the
438 developing gametocytes to either gender, a plausible hypothesis would be that the subset with smaller
439 nucleus represents immature female gametocytes, while cells with larger nucleus represent immature

440 male gametocytes. However, this is in conflict with a recent finding that commitment, as indicated by
441 measurable differences in gene expression, to either male or female cell fate is only decided at stage
442 III[79]. Furthermore, a recent study utilizing array tomography has found no such nuclear dimorphism in
443 earlier stages but does show the same similar dimorphism and absolute volumes to our findings for later
444 stages[15]. It would be interesting to see whether these different observations stem from differences in
445 experimental methods, stage assignment, image segmentation or biological material.

446 **Appositions of nucleus and endosymbiotic organelles**

447 In *Plasmodium*, both mitochondrion and apicoplast have essential organellar ribosomes, with promising
448 features as drug targets[80-83]. Nevertheless, neither have an associated set of organelle targeted tRNAs
449 that would be sufficient to facilitate translation of their respective genomes[84]. Recently, it has been
450 found that the nuclear-mitochondrial MCS play a role in RNA exchange and signaling. These sites are
451 distinct from the well-characterized peripheral ER-mitochondrial MCS but likewise enabled by tether
452 proteins without obvious homologues in the *Plasmodium* genome[85, 86]. We find distinct appositions of
453 the nucleus and mitochondrion in both early schizont and gametocytes (Fig. 6A, B). At these sites there
454 appears to be continuity of the outer leaflet of the nuclear envelope and the outer mitochondrial
455 membrane. In contrast, we find that the nucleus-apicoplast interface in ABS is characterized by a local
456 condensation of the normally spatially separated layers of the nuclear envelope into one electron
457 denser layer without obvious membrane fusion (Fig. 6B). Whereas the mitochondrion in gametocytes
458 closely envelops large areas of the apicoplast, only a subset of cells have close physical proximity
459 between nucleus and apicoplast and in those cells we never find indications of direct membrane
460 contact. Functionally, interfaces of apicoplast and mitochondrion with the nucleus might serve
461 phospholipid homeostasis or RNA exchange as has been suggested in model eukaryotes[85, 86], or provide
462 a potential mechanism for import of organellar tRNAs without known targeting signals thus shoring up
463 the incomplete translational machinery in these organelles.

464

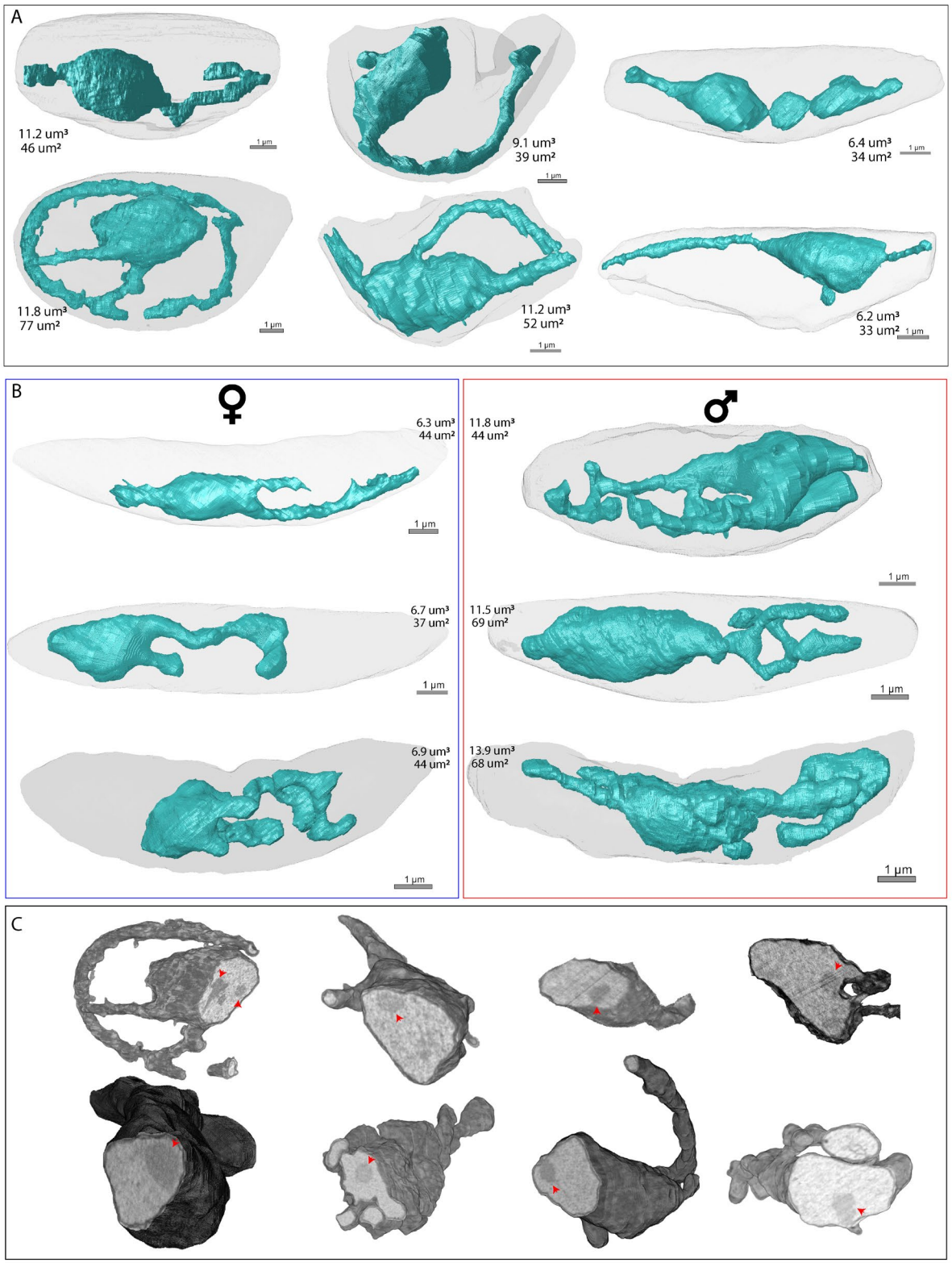

Figure 7 | **Distinct nuclear morphology in gametocytes**
Renderings of nuclei (teal) in stage II-III (**A**) and stage IV-V (**B**) gametocytes. Stage IV/V gametocytes are divided in female (blue outline) and male (red outline) gametocytes based on the number and appearance of osmiophilic bodies, hemozoin distribution and ER prevalence. For all nuclei, the respective volumes and surface areas are indicated. **C** Rendering of cross section of nuclei with grey values from EM data overlaid. Red arrowheads point at the position of the putative nucleolus.

Conclusion & Future Outlook

In this study, we applied volumetric electron microscopy to the transmittable gametocyte stages of the malaria parasite, allowing us to place findings from the past into their current molecular context and tackle questions that are challenging to address using single sections or serial sections with low z-resolution such as the connectivity within or between various organelles. Furthermore, these data allowed us to create the first 3D visualization of Golgi, gametocyte cytostome, Garnham body, and ER in gametocytes, improving our understanding of the cellular architecture in this part of the life cycle. In doing so, we are aware of the descriptive nature of this study and the limitations of the tool applied. Any of the hypotheses put forward are meant to provide a foundation for controlled molecular studies and targeted approaches that are more suitable to identify the underlying molecular players.

Public access and potential for reusability

FIB-SEM is a powerful tool, particularly for a cellular system that is as unusual as malaria parasites, as it allows determination of general ultrastructural organization and basic measurements to cover knowledge gaps that in other model eukaryotes have long been closed. Similar to other global datasets, one of the biggest challenges is to extract all relevant information and leverage the utility of non-targeted approaches and not just use them to answer one narrow question. To facilitate future re-interrogation of the data, we have deposited all underlying image stacks, as well as all analyzed cells and their corresponding segmentations, in the Electron Microscopy Public Image Archive (EMPIAR accession code XXXX). We hope that the latter can serve as training data for machine learning by groups with more suitable hardware/software and deep learning expertise to greatly simplify annotation workflows in the future.

Acknowledgements

We thank the molecular team members of the Malaria Research Group for fruitful discussions. We also thank Nico Sommerdijk and the EM center for supporting this work and Sabrina Absalon for critically proofreading the manuscript. F.E. and T.W.A.K. were supported by the Netherlands Organisation for Scientific Research (NWO-VIDI 864.13.009), C.B. by a PhD fellowship from the Radboud Institute for Molecular Life Sciences, Radboudumc (RIMLS018-009b).

Author contributions

F.E., R.R, M.K.L and C.B. performed experiments. R.E.S provided conceptual advice and analysis. F.E. analyzed the results, prepared illustrations and wrote the first manuscript draft. A.A. provided resources technical expertise and conceptual advice. T.W.A.K. contributed to conceptual development, provided resources and edited the manuscript. All authors contributed to data interpretation and provided feedback on the manuscript. All authors approved the final version of the manuscript.

510 **Textbox 1 Membrance contact sites**

511 Membrane contact sites (MCS) have typically been defined as areas of membranes of two organelles
512 that are in close proximity to each other. These areas can be homotypic (between the same type of
513 organelle, e.g. mitochondrion-mitochondrion MCS) or heterotypic (between different organelle types,
514 e.g. mitochondrion-ER MCS). To increase clarity and create a unified vocabulary Scorrano *et al.*[87] have
515 put together a set of unifying features that a MCS should have to be characterized as such.

516 1. There should be tethering forces from either protein-lipid or protein-protein interactions that
517 maintain the distance. This replaces previous proximity ranges that were used as guidelines as contact
518 sites have been found that far exceed these distance guidelines.

519 2. There should be no fusion of membranes. If there is fusion of membranes this can be referred to as
520 docking or fusion. Vesicular transport at the contact site may exist within this definition.

521 3. All contact sites should fulfil a specific function. A disruption of a contact site should impact cell
522 function.

523 4. MCS should have a defined proteome or lipidome that is required for their function, maintenance, or
524 regulation.

525 5. Time is not a factor. Dynamic or transient structures that fulfil the other requirements can be
526 considered a MCS.

527

528

529

530

531

532

533

534

535

536

537

538

539

540

541

542

543 **Materials & Methods**

544 **Parasite culture & gametocyte induction**

545 All parasite material used in this study is derived from the NF54/iGP2 strain. NF54/iGP2 parasites were
546 previously shown to be able successfully complete the whole lifecycle as well as not markedly differ
547 from wildtype NF54 parasites in other parameters that were investigated[78]. This parasite strain has the
548 desirable property that gametocytogenesis can be selectively induced by removal of glucosamine from
549 the medium, which triggers sexual commitment through the transcriptional cascade centered around
550 the AP2G gene[88]. Asexual blood-stage parasites (ABS) were maintained according to standard culturing
551 procedure in RPMI [7.4] supplemented with 10% human serum and 5% haematocrit using standard
552 culturing technique in a semi-automatic culturing system[5, 89]. For the maintenance of the NF54/iGP2
553 strain, an additional supplement of 2.5 mM D-(+)-glucosamine hydrochloride (Sigma #1514) was used.
554 To induce gametocytogenesis, glucosamine was omitted from the culturing medium. Between days 4
555 and 8 after gametocyte induction 50 mM N-acetylglucosamine (Sigma #A6525) was used to eliminate
556 ABS parasites. On day 14 gametocyte-infected RBCs were separated from uninfected RBCs through
557 magnetic separation as described previously[90]. Close attention was paid to prewarm and maintain all
558 solutions and apparatus at 37°C to avoid unintended activation of mature gametocytes. As reference
559 material trophozoite and schizont stages from mixed ABS cultures were similarly enriched through
560 magnetic separation and processed alongside the gametocyte cultures. For sample 3 N-
561 acetylglucosamine treatment was omitted to control for phenotypes causes by this treatment. This
562 omission leads to presence of ABS in the resulting images (sample 3).

563 **Sample preparation for electron microscopy**
564
565 Samples were prepared as described previously[20]. Briefly, the enriched infected red blood cells were
566 fixed using 2% glutaraldehyde in 0.1 M cacodylate (pH 7.4) buffer overnight at a temperature of 4 °C.
567 The fixed cells were then washed and the cell-pellet was resuspended in 3% ultra-low-gelling agarose,
568 solidified, and cut into small blocks. The agarose blocks containing the fixed cells were postfixed for
569 1 hour at room temperature using a solution of 2% osmium tetroxide and 1.5% potassium ferrocyanide
570 in 0.1 M cacodylate buffer containing 2 mM CaCl2, washed in MQ and then treated with 0.5%
571 thiocarbohydrazide for 30 minutes at room temperature. After washing, the agarose blocks were again
572 suspended in 2% osmium for 30 minutes at room temperature, washed, and then placed in a 2%
573 aqueous uranyl acetate solution overnight at 4 °C. The blocks were then washed and placed in a lead
574 aspartate solution (pH 5.5) for 30 minutes at 60 °C, washed, dehydrated using an ascending series of
575 aqueous ethanol solutions, and subsequently transferred via a mixture of aceton and Durcupan to pure
576 Durcupan (Sigma) as an embedding medium. The aforementioned staining procedure is primarily
577 optimized for high membrane contrast and staining of lipid-rich structures due by utilizing the
578 combination of potassium ferrocyanide, osmium tetroxide and thiocarbohydrazide[91]. Uranyl acetate
579 and lead aspartate furthermore stain DNA/RNA, proteins as well as carbohydrates[92, 93].

580 **FIB-SEM**
581 After polymerization and in order to create a smooth plane for FIB-SEM imaging, the sample surface was
582 smoothened using an ultra-microtome (Reichert Ultracut S ultramicrotome (Leica microsystems)). The
583 region of interest was cut out of the resin block and glued on an SEM stub with carbon tape, using
584 conductive silver paint. The samples were then coated with a gold sputter coater (Edwards, Stockholm,
585 Sweden) before introduction into a Zeiss Crossbeam 550 FIB-SEM (Carl Zeiss).

586 Multiple coarse trenches were milled using a 30 kV@30 nA probe to choose the regions of interest for
587 further 3D volume imaging. Parameters for serial sectioning imaging of large regions were set using the
588 Atlas 3D software (Atlas Engine v5.3.3). The large trenches were first smoothened using a 30 kV@1.5 nA
589 FIB probe, and thereafter a 30 kV@700 pA probe current was used for serial FIB milling. InLens
590 secondary and backscattered electron microscopy images were simultaneously collected at an
591 acceleration voltage of 2.0 kV with a probe current of 500 pA. The backscattered grid was set to −902 V.
592 For noise reduction, images were acquired using line average (n=1) and a dwell time of 3,0 µs. The
593 milling and imaging processes were continuously repeated and long series of images were acquired.
594

	Sample 1	Sample 2	Sample 3	Sample 4	Sample 5
Lifecycle Stage	GCT	GCT	GCT w/ ABS	ABS	ABS
Dimensions (x,y,z) [nm]	4268x2784x2293	4428x3804x952	4402x2850x900	4423x1430 x 1085	4010x3157x739
Total Volume Imaged [um^3]	10217	6013	4234	2573	3508

595 Table 1. Basic parameters of FIB-SEM stacks used in these studies. All samples constitute biological replicates.
596
597 **Serial sectioning**
598 To have a lower noise reference and identify potential FIB imaging artifacts one gametocyte sample was
599 also analyzed through serial sectioning combined with SEM. After checking for desired density of cells
600 with toluidine blue corresponding resin block was trimmed to the desired size and mounted onto the
601 chuck of a Leica Artos 3D Ultramicrotome. The block was sectioned into thin 80nm slices and sections
602 were collected onto Indium Tin Oxide glass coated with 5 nm carbon. The sections were then imaged
603 with a scanning electron microscope (Sigma300, Zeiss) at an acceleration voltage of 30 kV (HDBSD, 60
604 µm, high current) using Atlas 5 software. In total 47 consecutive images were taken leading to a total
605 imaged volume of 15124 um^3.
606
607 **Postprocessing and segmentation**
608 All processing, visualization and analysis performed in the ORS Dragonfly software (V2022.2).
609 Wherever necessary image stacks were aligned using the mutual information and sum of squared
610 differences registration method and results were manually controlled and adjusted whenever necessary.
611 Contrast was enhanced through application of contrast limited adaptive histogram equalization (CLAHE).
612 3D segmentation was performed using either manual segmentation or deep learning based
613 segmentation, based on which cellular feature was segmented. Deep-learning based segmentations
614 were controlled for errors and manually adjusted when necessary. For 3D rendering the segmented
615 regions of interest were converted to triangle meshes.
616
617 **Immunofluorescent assays**
618 To induce gametocytes, NF54 parasites were swapped from their earlier described complete culture
619 media to RPMI media supplemented with 0.5% Albumax (AlbuMAX II™, Thermo Fisher, #11021-037) at
620 26 hours post invasion. The parasites were allowed to commit for 36 hours, before being put back on
621 complete culture media. At day 12 post induction, stage V gametocytes were stained in 100 nM
622 MitoTracker (MitoTracker® Orange CMTMRos, Thermo Fisher, #M7510) diluted in complete media at
623 37°C for 30 minutes. Stage V gametocyte samples were diluted 1:10 in warm complete media before
624 being allowed to settle on pre-heated Poly-L-Lysine coated coverslips (Corning, #354085) for 15 minutes
625 at 37°C, while activated gamete samples were mixed 1:1 with in 30µM xanthurenic acid (Sigma Aldrich,
626 #D120804) and subsequently settled for 15 minutes at RT. Both samples were fixed with 4%
627 paraformaldehyde (Thermo Fisher, #28906)) and 0.0075% glutaraldehyde (Panreac, #A0589,0010) in
628 PBS for 20 minutes at RT. The fixed samples were, permeabilised with 0.1% Triton X-100 in PBS for 10
629 minutes and blocked in 3% BSA (Sigma Aldrich, #A9418) for 1 hour at RT. To differentiate between male

630 and female gametocytes, the samples were stained with primary α-Tubulin antibody (Thermo Fisher,
631 #MA1-19162) for 1 hour at RT, which was visualised with Donkey anti-Mouse Alexa Fluor™ 647 (Thermo
632 Fisher, #A-31571). Finally, samples were stained with 300 nM DAPI (Thermo Fisher, #62248) for 30
633 minutes at RT before being mounted on a microscope slide using VECTASHIELD (VWR, #H-1000) and
634 sealed in nail polish. The samples were imaged on an confocal LSM900 microscope with airyscan (Zeiss).
635 Z-stack images were obtained with a 0.14 µm step size. Laser power and detector sensibility are
636 maintained the same throughout all the images. A maximum projection was created for every image, in
637 which the tubulin signal was pre-set in order to differentiate between male and female gametocytes.
638
639
640
641
642
643
644
645
646
647
648
649
650
651
652
653
654
655
656
657
658
659
660
661
662

663 **Literature**

664 1. World Health, O. World malaria report 2021. (World Health Organization, Geneva; 2021).
665 2. Organization, W.H. World malaria report 2022. (World Health Organization, 2022).
666 3. Monroe, A., Williams, N.A., Ogoma, S., Karema, C. & Okumu, F. Reflections on the 2021 World
667 Malaria Report and the future of malaria control. *Malaria Journal* **21**, 154 (2022).
668 4. Munro, B.A. & McMorran, B.J. in Parasitologia, Vol. 2 101-124 (2022).
669 5. Ponnudurai, T., Lensen, A.H.W., Meis, J.F.G.M. & Meuwissen, J.H.E.T. Synchronization of
670 Plasmodium falciparum gametocytes using an automated suspension culture system.
671 *Parasitology* **93**, 263-274 (1986).
672 6. Sinden, R.E., Canning, E.U., Bray, R.S., Smalley, M.E. & Garnham, P.C.C. Gametocyte and gamete
673 development in Plasmodium falciparum. *Proceedings of the Royal Society of London. Series B.*
674 *Biological Sciences* **201**, 375-399 (1978).
675 7. Langreth, S.G. Electron microscope cytochemistry of host-parasite membrane interactions in
676 malaria. *Bull World Health Organ* **55**, 171-178 (1977).
677 8. Kass, L., Willerson, D., Rieckmann, K., Carson, P. & Becker, R. Plasmodium Falciparum
678 Gametocytes: Electron Microscopic Observations on Material Obtained by a New Method. *The*
679 *American journal of tropical medicine and hygiene* **20**, 187-194 (1971).
680 9. Bannister, L.H., Hopkins, J.M., Fowler, R.E., Krishna, S. & Mitchell, G.H. Ultrastructure of rhoptry
681 development in Plasmodium falciparum erythrocytic schizonts. *Parasitology* **121**, 273-287
682 (2000).
683 10. Bannister, L.H., Hopkins, J.M., Margos, G., Dluzewski, A.R. & Mitchell, G.H. Three-Dimensional
684 Ultrastructure of the Ring Stage of Plasmodium falciparum: Evidence for Export Pathways.
685 *Microscopy and Microanalysis* **10**, 551-562 (2004).
686 11. Sinden, R.E. & Strong, K. An ultrastructural study of the sporogonic development of Plasmodium
687 falciparum in Anopheles gambiae. *Transactions of the Royal Society of Tropical Medicine and*
688 *Hygiene* **72**, 477-491 (1978).
689 12. Slomianny, C., Prensier, G. & Charet, P. Ingestion of erythrocytic stroma by Plasmodium
690 chabaudi trophozoites: ultrastructural study by serial sectioning and 3-dimensional
691 reconstruction. *Parasitology* **90 (Pt 3)**, 579-588 (1985).
692 13. Rudlaff, R.M., Kraemer, S., Marshman, J. & Dvorin, J.D. Three-dimensional ultrastructure of
693 Plasmodium falciparum throughout cytokinesis. *PLOS Pathogens* **16**, e1008587 (2020).
694 14. Araki, T. et al. Three-dimensional electron microscopy analysis reveals endopolygeny-like
695 nuclear architecture segregation in Plasmodium oocyst development. *Parasitology International*
696 **76**, 102034 (2020).
697 15. Li, J. et al. Repurposing the mitotic machinery to drive cellular elongation and chromatin
698 reorganisation in Plasmodium falciparum gametocytes. *Nature Communications* **13**, 5054
699 (2022).
700 16. Parkyn Schneider, M. et al. Disrupting assembly of the inner membrane complex blocks
701 Plasmodium falciparum sexual stage development. *PLoS Pathog* **13**, e1006659 (2017).
702 17. Rashpa, R. & Brochet, M. Expansion microscopy of Plasmodium gametocytes reveals the
703 molecular architecture of a bipartite microtubule organisation centre coordinating mitosis with
704 axoneme assembly. *PLOS Pathogens* **18**, e1010223 (2022).
705 18. Matz, J.M., Goosmann, C., Matuschewski, K. & Kooij, T.W.A. An Unusual Prohibitin Regulates
706 Malaria Parasite Mitochondrial Membrane Potential. *Cell Reports* **23**, 756-767 (2018).
707 19. Okamoto, N., Spurck Timothy, P., Goodman Christopher, D. & McFadden Geoffrey, I. Apicoplast
708 and Mitochondrion in Gametocytogenesis of Plasmodium falciparum. *Eukaryotic Cell* **8**, 128-132
709 (2009).

710 20. Evers, F. et al. Composition and stage dynamics of mitochondrial complexes in Plasmodium
711 falciparum. *Nat Commun* **12**, 3820 (2021).
712 21. Krungkrai, S.R., Learngaramkul, P., Kudan, S., Prapunwattana, P. & Krungkrai, J. Mitochondrial
713 heterogeneity in human malarial parasite Plasmodium falciparum. *Science Asia* **25**, 77-83 (1999).
714 22. Sinden, R.E. Gametocytogenesis of Plasmodium falciparum in vitro: an electron microscopic
715 study. *Parasitology* **84**, 1-11 (1982).
716 23. de Koning-Ward, T.F. et al. The role of osmiophilic bodies and Pfg377 expression in female
717 gametocyte emergence and mosquito infectivity in the human malaria parasite Plasmodium
718 falciparum. *Mol Microbiol* **67**, 278-290 (2008).
719 24. Olivieri, A. et al. Distinct properties of the egress-related osmiophilic bodies in male and female
720 gametocytes of the rodent malaria parasite Plasmodium berghei. *Cell Microbiol* **17**, 355-368
721 (2015).
722 25. Aikawa, M., Huff, C.G. & Sprinz, H. Comparative fine structure study of the gametocytes of avian,
723 reptilian, and mammalian malarial parasites. *Journal of Ultrastructure Research* **26**, 316-331
724 (1969).
725 26. Sassmannshausen, J. et al. Comparative proteomics of vesicles essential for the egress of
726 Plasmodium falciparum gametocytes from red blood cells. *bioRxiv*,
727 2023.2002.2008.527640 (2023).
728 27. Liu, B. et al. Multimodal analysis of Plasmodium knowlesi-infected erythrocytes reveals large
729 invaginations, swelling of the host cell, and rheological defects. *Cellular Microbiology* **21**, e13005
730 (2019).
731 28. Garnham, P.C.C. Malaria parasites and other Haemosporidia. *Malaria Parasites and other*
732 *Haemosporidia.* (1966).
733 29. Petter, M., Bonow, I. & Klinkert, M.-Q. Diverse Expression Patterns of Subgroups of the rif
734 Multigene Family during Plasmodium falciparum Gametocytogenesis. *PLOS ONE* **3**, e3779
735 (2008).
736 30. Garnham, P. On Some Curious Bodies found in Erythrocytes containing Immature Crescents.
737 *Transactions of the Royal Society of Tropical Medicine and Hygiene* **26** (1933).
738 31. Orjih, A.U. Hemozoin accumulation in Garnham bodies of Plasmodium falciparum gametocytes.
739 *Parasitology Research* **111**, 2353-2359 (2012).
740 32. Raventos-Suarez, C., Kaul, D.K., Macaluso, F. & Nagel, R.L. Membrane knobs are required for the
741 microcirculatory obstruction induced by Plasmodium falciparum-infected erythrocytes.
742 *Proceedings of the National Academy of Sciences* **82**, 3829-3833 (1985).
743 33. Quadt, K.A. et al. The density of knobs on Plasmodium falciparum-infected erythrocytes
744 depends on developmental age and varies among isolates. *PLoS One* **7**, e45658 (2012).
745 34. Milani, K.J., Schneider, T.G. & Taraschi, T.F. Defining the morphology and mechanism of the
746 hemoglobin transport pathway in Plasmodium falciparum-infected erythrocytes. *Eukaryot Cell*
747 **14**, 415-426 (2015).
748 35. Xie, S.C., Ralph, S.A. & Tilley, L. K13, the Cytostome, and Artemisinin Resistance. *Trends in*
749 *Parasitology* **36**, 533-544 (2020).
750 36. Tran, P.N. et al. Changes in lipid composition during sexual development of the malaria parasite
751 Plasmodium falciparum. *Malar J* **15**, 73 (2016).
752 37. Mathur, J., Kroeker, O.F., Lobbezoo, M. & Mathur, N. The ER Is a Common Mediator for the
753 Behavior and Interactions of Other Organelles. *Frontiers in Plant Science* **13** (2022).
754 38. Khan, S.M. et al. Proteome Analysis of Separated Male and Female Gametocytes Reveals Novel
755 Sex-Specific Plasmodium Biology. *Cell* **121**, 675-687 (2005).
756 39. Janse, C. & Waters, A. Sexual development of malaria parasites. (Norwich: Horizon Scientific
757 Press, 2004).

758 40. Adisa, A. et al. Re-assessing the locations of components of the classical vesicle-mediated
759 trafficking machinery in transfected Plasmodium falciparum. *International journal for*
760 *parasitology* **37**, 1127-1141 (2007).
761 41. Krai, P., Dalal, S. & Klemba, M. Evidence for a Golgi-to-Endosome Protein Sorting Pathway in
762 Plasmodium falciparum. *PLOS ONE* **9**, e89771 (2014).
763 42. Hallée, S. et al. Identification of a Golgi apparatus protein complex important for the asexual
764 erythrocytic cycle of the malaria parasite Plasmodium falciparum. *Cell Microbiol* **20**, e12843
765 (2018).
766 43. Jonsdottir, T.K., Gabriela, M., Crabb, B.S., F. de Koning-Ward, T. & Gilson, P.R. Defining the
767 Essential Exportome of the Malaria Parasite. *Trends in Parasitology* **37**, 664-675 (2021).
768 44. Alano, P. Plasmodium falciparum gametocytes: still many secrets of a hidden life. *Molecular*
769 *Microbiology* **66**, 291-302 (2007).
770 45. Tibúrcio, M. et al. Early gametocytes of the malaria parasite Plasmodium falciparum specifically
771 remodel the adhesive properties of infected erythrocyte surface. *Cell Microbiol* **15**, 647-659
772 (2013).
773 46. Beck, J., Muralidharan, V., Oksman, A. & Goldberg, D. PTEX component HSP101 mediates export
774 of diverse malaria effectors into host erythrocytes. *Nature* **511** (2014).
775 47. Jennison, C. et al. Inhibition of Plasmepsin V Activity Blocks Plasmodium falciparum
776 Gametocytogenesis and Transmission to Mosquitoes. *Cell Reports* **29**, 3796-3806.e3794 (2019).
777 48. Matthews, K. et al. The Plasmodium translocon of exported proteins (PTEX) component
778 thioredoxin-2 is important for maintaining normal blood-stage growth. *Molecular Microbiology*
779 **89**, 1167-1186 (2013).
780 49. Ngotho, P. et al. Revisiting gametocyte biology in malaria parasites. *FEMS Microbiology Reviews*
781 **43**, 401-414 (2019).
782 50. Dearnley, M.K. et al. Origin, composition, organization and function of the inner membrane
783 complex of Plasmodium falciparum gametocytes. *J Cell Sci* **125**, 2053-2063 (2012).
784 51. Mühleip, A. et al. ATP synthase hexamer assemblies shape cristae of Toxoplasma mitochondria.
785 *Nature Communications* **12**, 120 (2021).
786 52. Hanssen, E., Goldie, K.N. & Tilley, L. Ultrastructure of the asexual blood stages of Plasmodium
787 falciparum. *Methods Cell Biol* **96**, 93-116 (2010).
788 53. Evers, F. et al. Composition and stage dynamics of mitochondrial complexes in Plasmodium
789 falciparum. *Nature Communications* **12**, 3820 (2021).
790 54. Uyemura, S.A., Luo, S., Moreno, S.N. & Docampo, R. Oxidative phosphorylation, Ca2+ transport,
791 and fatty acid-induced uncoupling in malaria parasites mitochondria. *Journal of Biological*
792 *Chemistry* **275**, 9709-9715 (2000).
793 55. Wolf, S.G. et al. 3D visualization of mitochondrial solid-phase calcium stores in whole cells. *Elife*
794 **6** (2017).
795 56. Goldfischer, S., Kress, Y., Coltoff-Schiller, B. & Berman, J. Primary fixation in osmium-potassium
796 ferrocyanide: the staining of glycogen, glycoproteins, elastin, an intranuclear reticular structure,
797 and intercisternal trabeculae. *J Histochem Cytochem* **29**, 1105-1111 (1981).
798 57. Kacem, H., Giese, E.G. & Miquel, J. Sperm characters in the Hemiuridae (Digenea): first data on
799 Aphanurus stossichii (Aphanurinae) and Ectenurus lepidus (Dinurinae). *Parasitology Research*
800 **119**, 991-999 (2020).
801 58. Rey, T. et al. Mitochondrial RNA granules are fluid condensates positioned by membrane
802 dynamics. *Nature Cell Biology* **22**, 1180-1186 (2020).
803 59. Atkinson, A. & Winge, D.R. Metal Acquisition and Availability in the Mitochondria. *Chemical*
804 *Reviews* **109**, 4708-4721 (2009).

60. Cohen, M.M. & Tareste, D. Recent insights into the structure and function of Mitofusins in mitochondrial fusion. *F1000Research* **7** (2018).
61. Kudryashev, M. et al. Positioning of large organelles by a membrane-associated cytoskeleton in Plasmodium sporozoites. *Cellular microbiology* **12**, 362-371 (2010).
62. Stanway, R.R. et al. Organelle segregation into Plasmodium liver stage merozoites. *Cellular Microbiology* **13**, 1768-1782 (2011).
63. Kobayashi, T. et al. Mitochondria and apicoplast of Plasmodium falciparum: behaviour on subcellular fractionation and the implication. *Mitochondrion* **7**, 125-132 (2007).
64. Sato, S., Clough, B., Coates, L. & Wilson, R.J. Enzymes for heme biosynthesis are found in both the mitochondrion and plastid of the malaria parasite Plasmodium falciparum. *Protist* **155**, 117-125 (2004).
65. Sheiner, L., Vaidya, A.B. & McFadden, G.I. The metabolic roles of the endosymbiotic organelles of Toxoplasma and Plasmodium spp. *Current Opinion in Microbiology* **16**, 452-458 (2013).
66. Wu, H., Carvalho, P. & Voeltz, G.K. Here, there, and everywhere: The importance of ER membrane contact sites. *Science* **361**, eaan5835 (2018).
67. Lee, S. & Min, K.T. The Interface Between ER and Mitochondria: Molecular Compositions and Functions. *Mol Cells* **41**, 1000-1007 (2018).
68. Burgoyne, T., Patel, S. & Eden, E.R. Calcium signaling at ER membrane contact sites. *Biochimica et Biophysica Acta (BBA) - Molecular Cell Research* **1853**, 2012-2017 (2015).
69. de Brito, O.M. & Scorrano, L. Mitofusin 2 tethers endoplasmic reticulum to mitochondria. *Nature* **456**, 605-610 (2008).
70. Voleman, L. & Doležal, P. Mitochondrial dynamics in parasitic protists. *PLoS Pathog* **15**, e1008008 (2019).
71. Elbaz-Alon, Y. et al. Lam6 Regulates the Extent of Contacts between Organelles. *Cell Reports* **12**, 7-14 (2015).
72. Santos, H.J. & Nozaki, T. Interorganellar communication and membrane contact sites in protozoan parasites. *Parasitology International* **83**, 102372 (2021).
73. Lahiri, S. et al. A conserved endoplasmic reticulum membrane protein complex (EMC) facilitates phospholipid transfer from the ER to mitochondria. *PLoS biology* **12**, e1001969 (2014).
74. Jumper, J. et al. Highly accurate protein structure prediction with AlphaFold. *Nature* **596**, 583-589 (2021).
75. Zardecki, C. et al. PDB-101: Educational resources supporting molecular explorations through biology and medicine. *Protein Science* **31**, 129-140 (2022).
76. Araiso, Y. et al. Structure of the mitochondrial import gate reveals distinct preprotein paths. *Nature* **575**, 395-401 (2019).
77. Webster, M., Witkin, K.L. & Cohen-Fix, O. Sizing up the nucleus: nuclear shape, size and nuclear-envelope assembly. *J Cell Sci* **122**, 1477-1486 (2009).
78. Boltryk, S.D. et al. CRISPR/Cas9-engineered inducible gametocyte producer lines as a valuable tool for Plasmodium falciparum malaria transmission research. *Nature Communications* **12**, 4806 (2021).
79. Gomes, A.R. et al. A transcriptional switch controls sex determination in Plasmodium falciparum. *Nature* **612**, 528-533 (2022).
80. Hollin, T. et al. Functional genomics of RAP proteins and their role in mitoribosome regulation in Plasmodium falciparum. *Nature Communications* **13**, 1275 (2022).
81. Ling, L. et al. Genetic ablation of the mitoribosome in the malaria parasite Plasmodium falciparum sensitizes it to antimalarials that target mitochondrial functions. *Journal of Biological Chemistry* **295**, 7235-7248 (2020).

852 82. Ke, H., Dass, S., Morrisey, J.M., Mather, M.W. & Vaidya, A.B. The mitochondrial ribosomal
853 protein L13 is critical for the structural and functional integrity of the mitochondrion in
854 Plasmodium falciparum. *Journal of Biological Chemistry* **293**, 8128-8137 (2018).
855 83. Dass, S. et al. Transcriptional changes in Plasmodium falciparum upon conditional knock down of
856 mitochondrial ribosomal proteins RSM22 and L23. *PLOS ONE* **17**, e0274993 (2022).
857 84. Vaidya, A.B. & Mather, M.W. Mitochondrial Evolution and Functions in Malaria Parasites. *Annual*
858 *Review of Microbiology* **63**, 249-267 (2009).
859 85. Eisenberg-Bord, M. et al. Cnm1 mediates nucleus-mitochondria contact site formation in
860 response to phospholipid levels. *J Cell Biol* **220** (2021).
861 86. Desai, R. et al. Mitochondria form contact sites with the nucleus to couple prosurvival
862 retrograde response. *Science Advances* **6**, eabc9955.
863 87. Scorrano, L. et al. Coming together to define membrane contact sites. *Nature Communications*
864 **10**, 1287 (2019).
865 88. Filarsky, M. et al. GDV1 induces sexual commitment of malaria parasites by antagonizing HP1-
866 dependent gene silencing. *Science* **359**, 1259-1263 (2018).
867 89. Trager, W. & Jensen, J.B. Human malaria parasites in continuous culture. *Science* **193**, 673-675
868 (1976).
869 90. Ribaut, C. et al. Concentration and purification by magnetic separation of the erythrocytic stages
870 of all human Plasmodium species. *Malaria journal* **7**, 1-5 (2008).
871 91. Willingham, M.C. & Rutherford, A.V. The use of osmium-thiocarbohydrazide-osmium (OTO) and
872 ferrocyanide-reduced osmium methods to enhance membrane contrast and preservation in
873 cultured cells. *Journal of Histochemistry & Cytochemistry* **32**, 455-460 (1984).
874 92. Reynolds, E.S. The use of lead citrate at high pH as an electron-opaque stain in electron
875 microscopy. *J Cell Biol* **17**, 208-212 (1963).
876 93. Huxley, H.E. & Zubay, G. Preferential Staining of Nucleic Acid-Containing Structures for Electron
877 Microscopy. *The Journal of Biophysical and Biochemical Cytology* **11**, 273-296 (1961).

878

Supplementary Figures

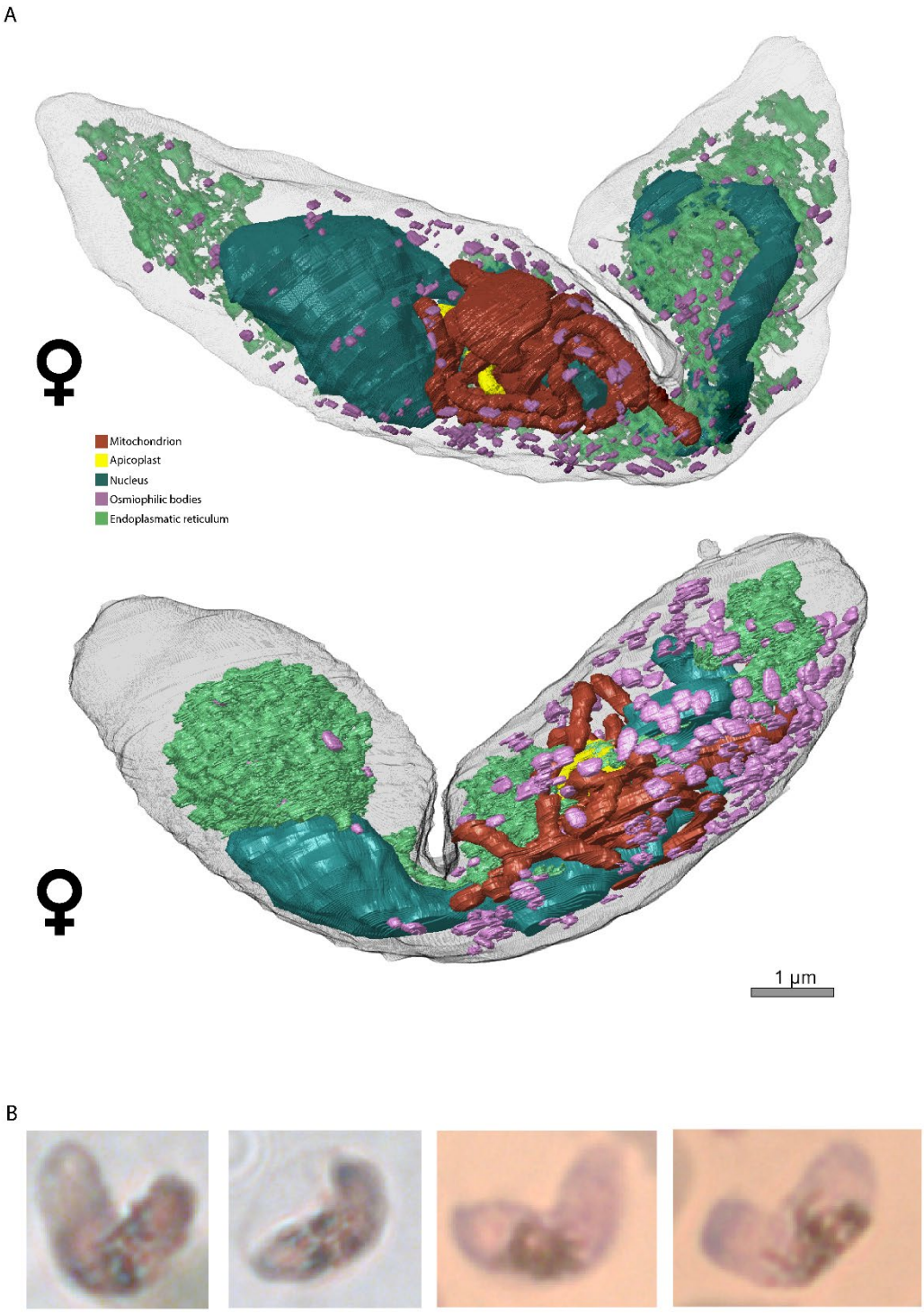

Supp. Figure 1. **Ultrastructural features of contorted mature female gametocytes**
A. Renderings of two contorted mature female gametocytes with a typical contorted appearance observed in gametocyte cultures. Ultrastructural features shown include nucleus, mitochondrion, ER, Golgi, osmiophilic bodies, and apicoplast. **B.** Exemplary crops from Giemsa-stained smears of gametocyte cultures showing mature female gametocytes with similar knicked appearance.

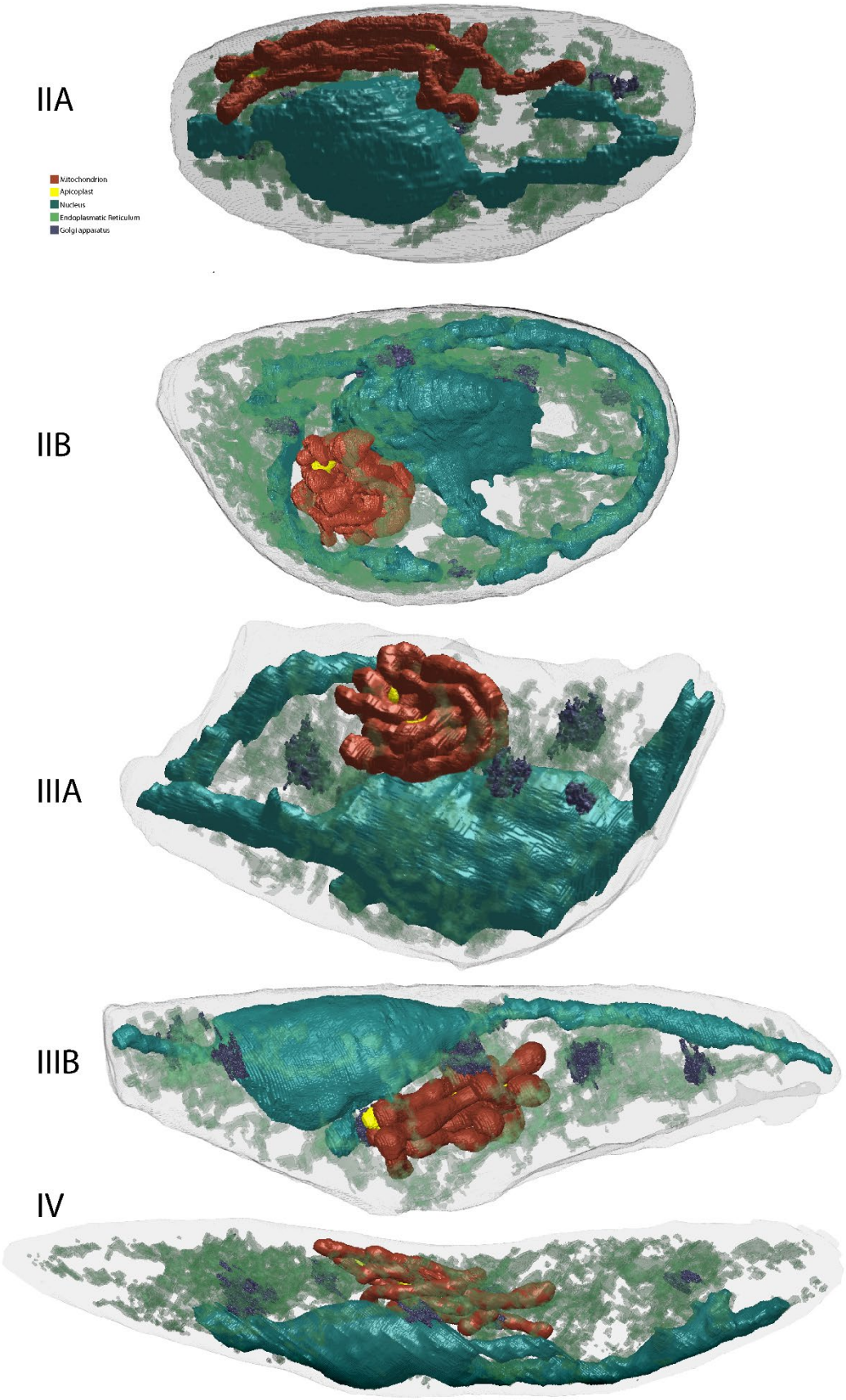

Supp. Figure 2. **Ultrastructural features of gametocytes in different developmental stages.**
Renderings of gametocytes in different developmental stages showing nucleus, mitochondrion, ER, Golgi apparatus, and apicoplast. ER rendering was made slightly transparent to allow better visibility of other features. Classifications were made based on cellular features typically associated with the respective developmental stages such as IMC cover or morphology of the parasite.

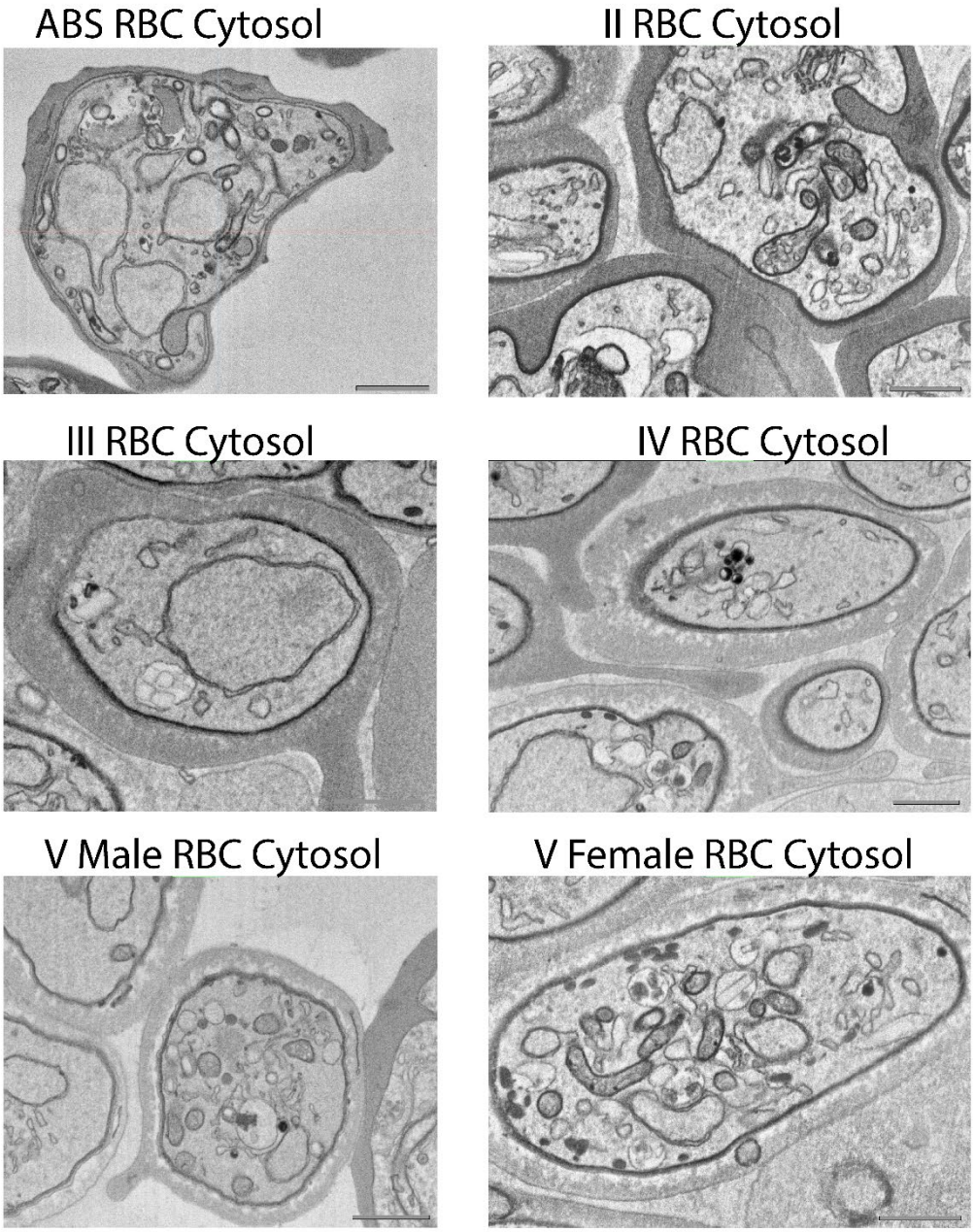

Supp. Figure 3. **Differing appearance of RBC cytoplasm in ABS, different gametocyte developmental stages**
While RBCs infected with ABS and stage II gametocytes contain a homogenous and relatively more electron dense cytoplasm**.** Starting in stage III the cytoplasm becomes increasingly electron lucent and an even more electron lucent corona starts to develop around and in close proximity to the gametocyte.

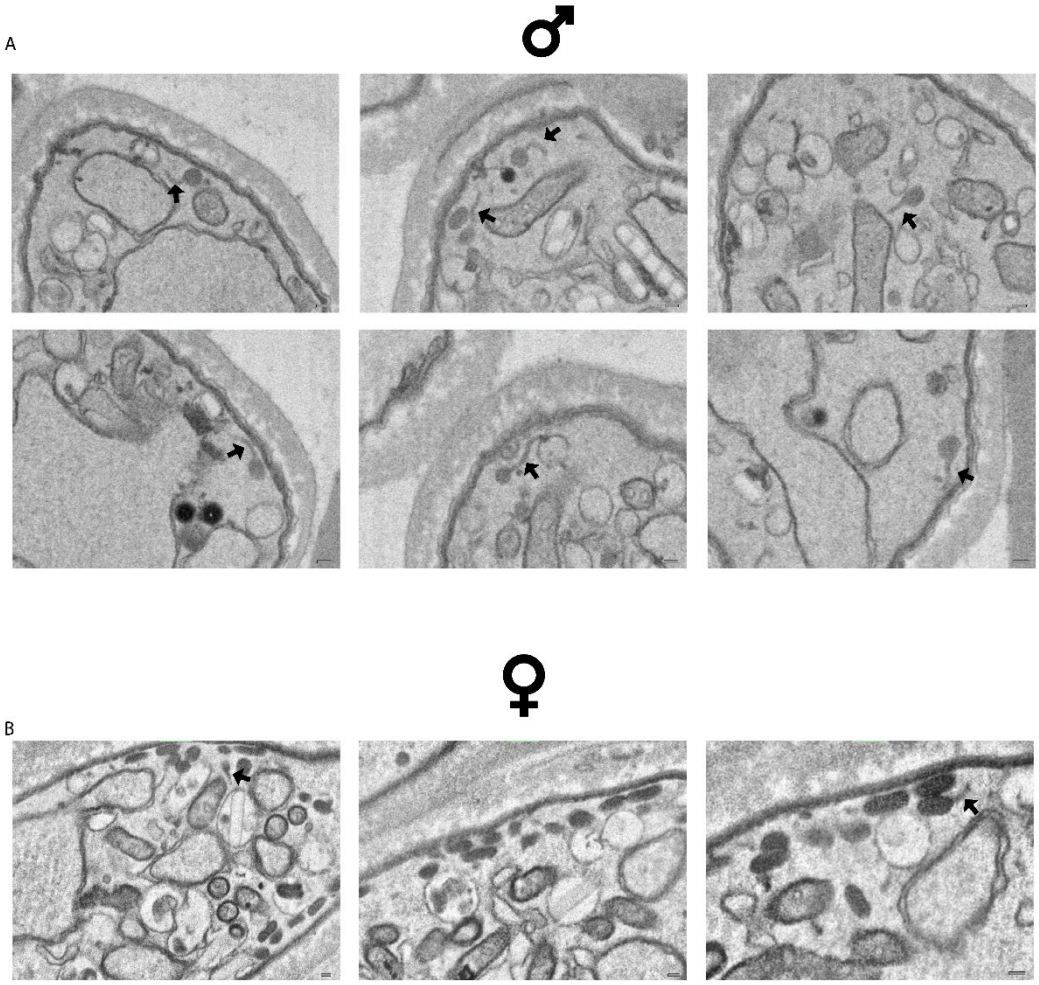

Supp. Figure 4. **Sex-specific differences in appearance of osmiophilic body-like structures.** Male gametocytes contain vesicles that resemble osmiophilic bodies in their appearance, but with a tail-like appendix. These structures are only occasionally observed in female gametocytes. Exemplary micrographs showing typical OB morphology in male (**A**) or female (**B**) gametocytes. Note that most OBs observed in female gametocytes do not have tail extensions while the vast majority or all of the OBs observed in male gametocytes possess tail extensions. Arrows point at tail extensions. Scale bars = 0.1 µm

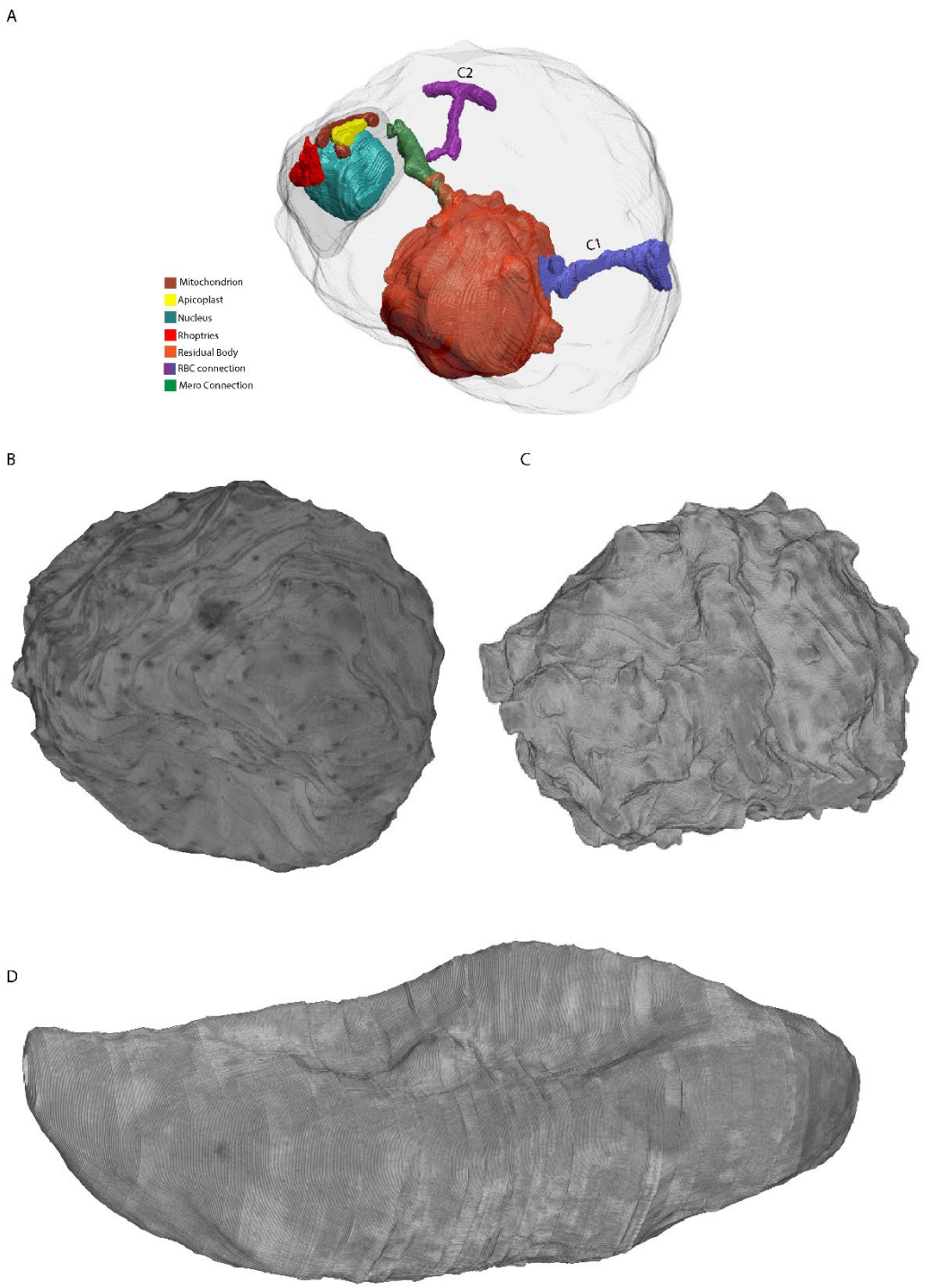

Supp. Figure 5 **Additional features of ABS A** A segmented schizont harbours long tubular connections between the residual body and the RBC cytoplasm (C1, C2) and a daughter merozoite. **B/C/D** Morphology of RBC infected by developing schizont, segmented schizont and mature gametocyte with grey values from the underlying EM data.

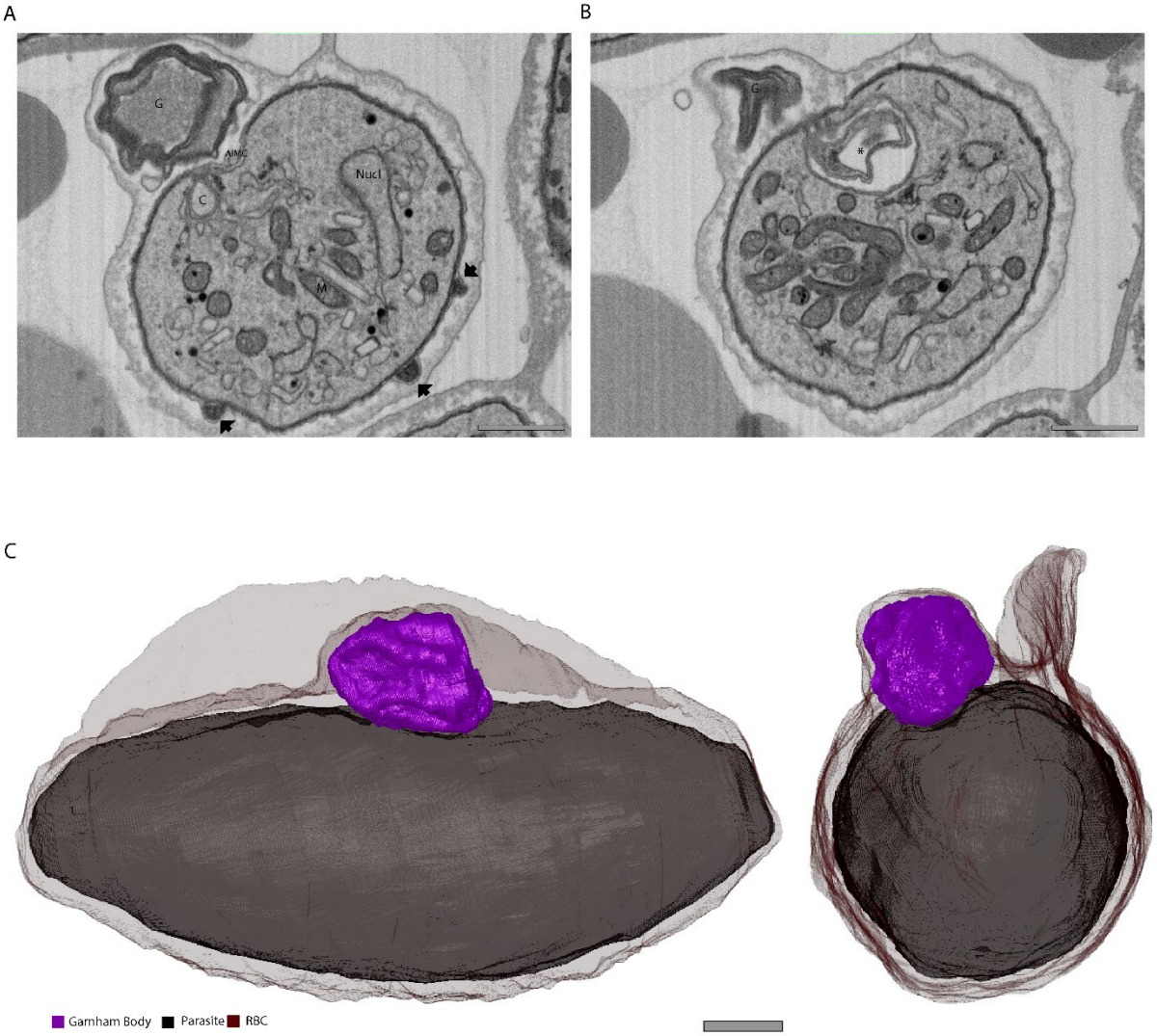

Supp. Figure 6 **The Garnham body A** Exemplary micrograph showing membrane makeup of the Garnham body (G) and the presence of a cytostome (C), local lack of IMC (ΔIMC) and cellular protrusion (arrow) **B** Exemplary micrograph showing aberrant internal structure opposing the Garnham body in the RBC (*) **C** Rendering of Garnham body from two angles. Scale bar = 1 µm

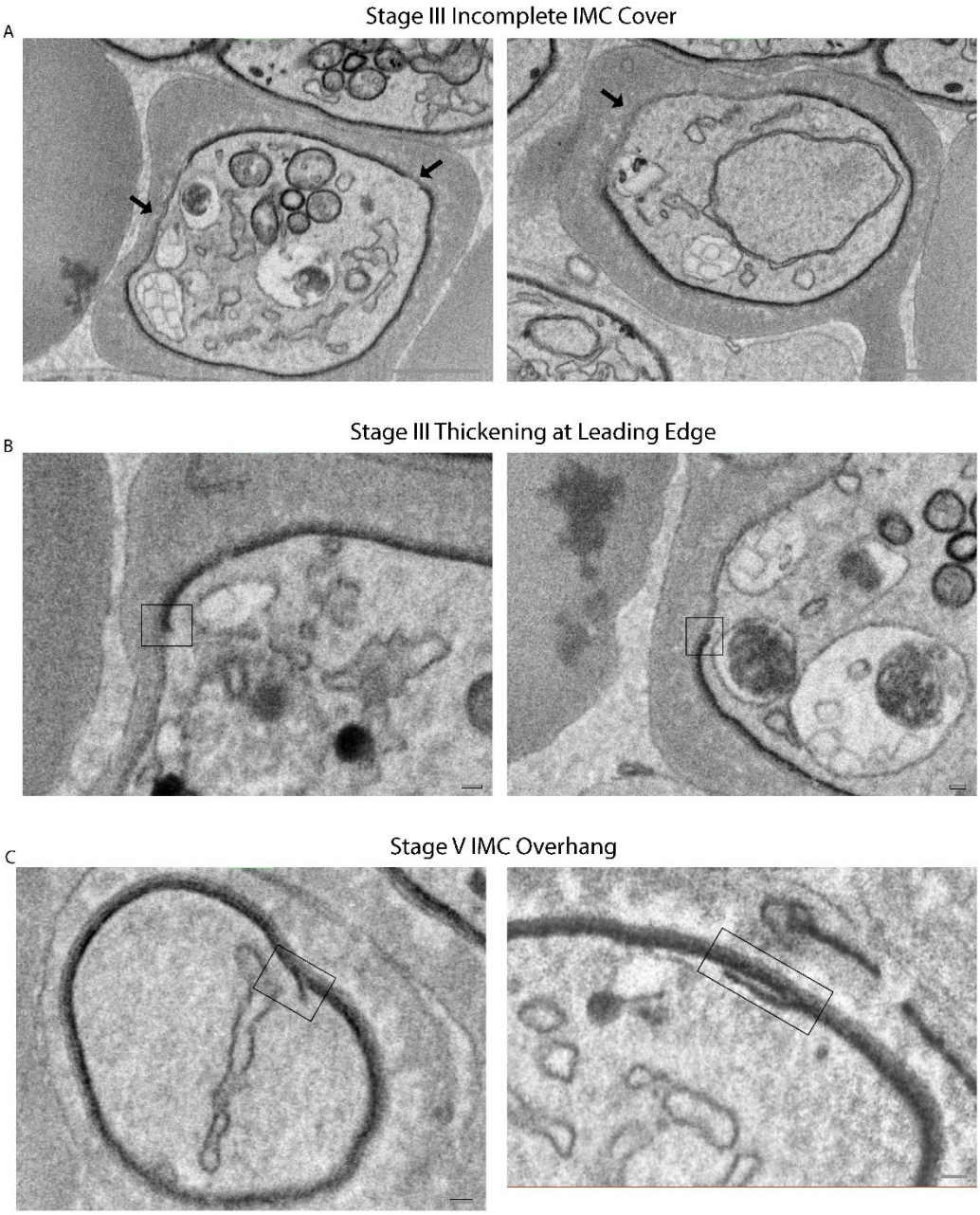

Supp Figure 7. **IMC features in stage III and stage V gametocytes A** Micrographs with examples of incomplete IMC cover in stage III gametocytes highlighted with arrows. Scale bar = 1 µm **B** Putative local thickening of IMC as described by Schneider et al. within boxes. Scale bar = 0.1 µm **C** IMC overhangs observed at polar ends of mature gametocytes. Scale bar = 0.1 µm

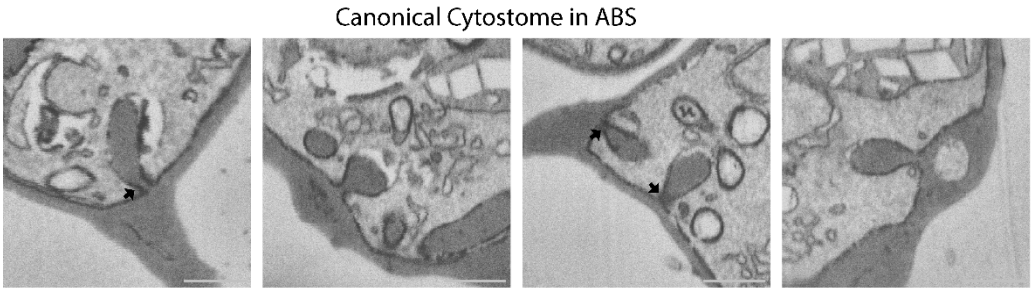

Supp. Figure 8 **The canonical cytostome** Example micrographs of the cytostome from various trophozoite or schizont stage parasites. Arrows highlight cytostomal collar. Scale bar = 1 µm

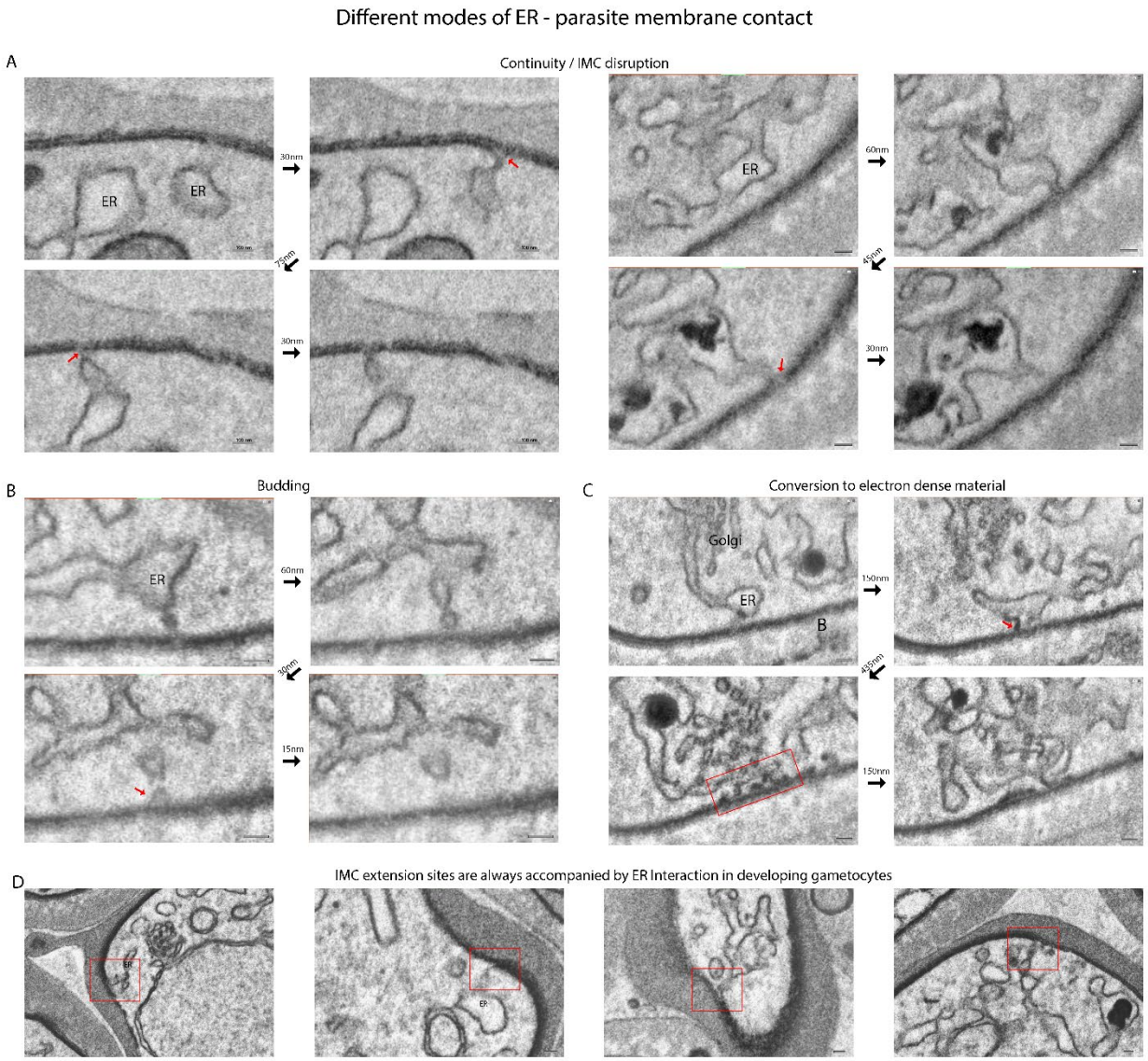

Supp Figure 9 **Interactions between ER and parasite membrane A / B / C** Series of micrographs from mature gametocytes showing ER in different putative interactions with the parasite membrane. **A** The ER directly contacts and forms a continuity with the IMC, leading to a local disruption of the IMC. **B** Same as **A** but connecting piece seemingly buds off from ER. **C** ER is continuous with electron dense material that contacts the IMC. Scale bar = 0.1 µm, Black arrows between images express distance in the z-axis (acquisition plane) from one slice to the other **D** Exemplary micrographs showing contact of ER with the four IMC extension sites that could be identified in a developing gametocyte. Scale bar = 0.1 µm

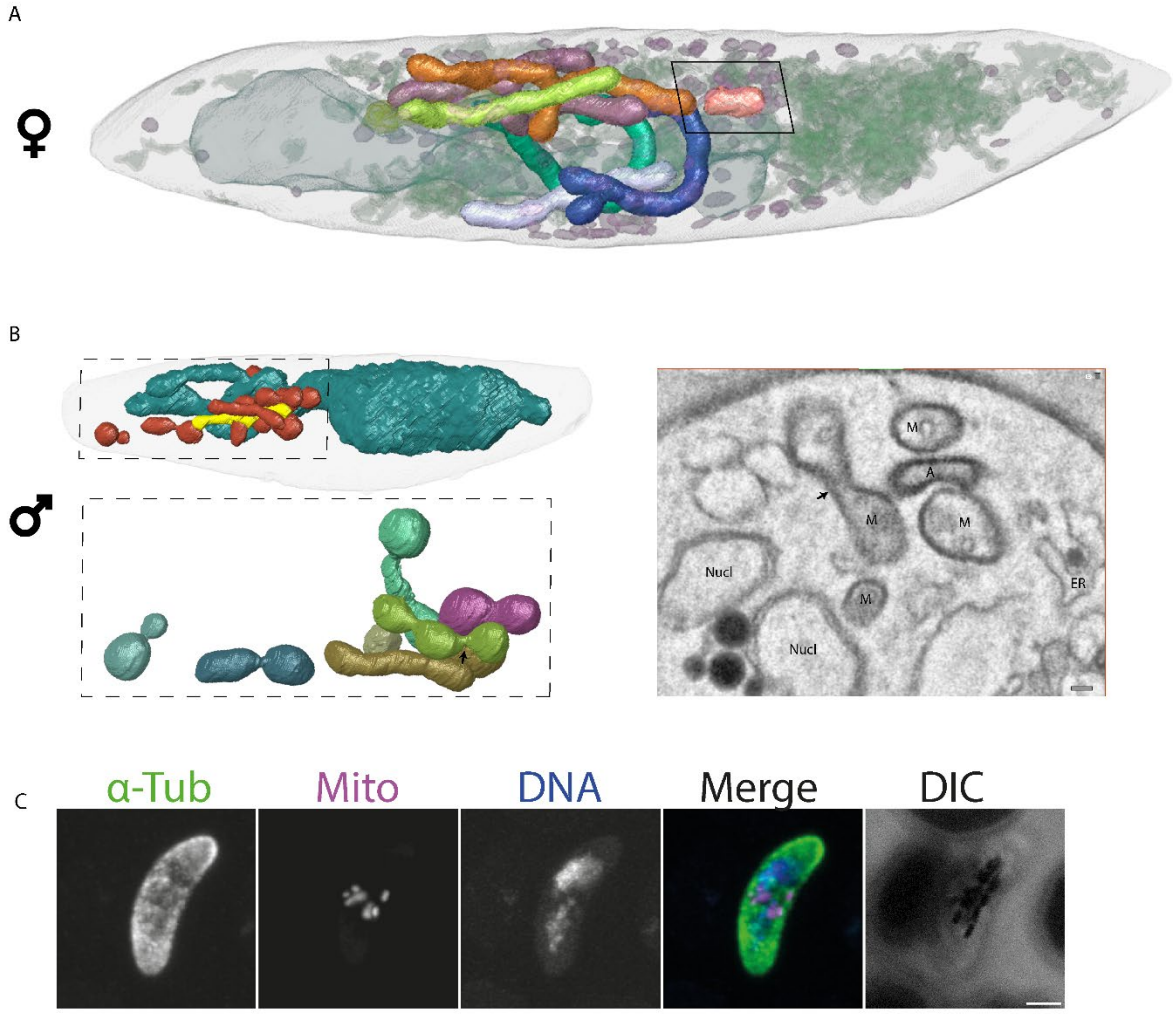

Supp. Figure 10 **Eloboration on multiple mitochondria in gametocytes**
A Rendering of a stage IV female gametocyte. Each of the seven mitochondria rendered in a separate color. One small mitochondrion is clearly recognizable as removed from the remainder (black rectangle). Nucleus, osmiophilic bodies, ER and apicoplast are rendered with high transparency to provide cellular context. **B** Rendering of nucleus, apicoplast and dispersed mitochondria (top left), a zoom of only mitochondria without cellular context (bottom left) as well as exemplary micrograph showing atypical mitochondrial morphology and constriction site (black arrow). **C** Immunofluorescence analysis of a mature male gametocyte. Depicted left to right are maximum intensity projections using anti-α-tubulin antibodies, MitoTracker™ , DAPI, merge of all channels and differential interference contrast (DIC) images. α-tubulin was used to distinguish male and female gametocytes, DNA was visualized using DAPI and mitochondria were visualized using MitoTracker. Mitochondrial staining suggests presence of multiple dispersed mitochondria. Scale bar = 2 µm

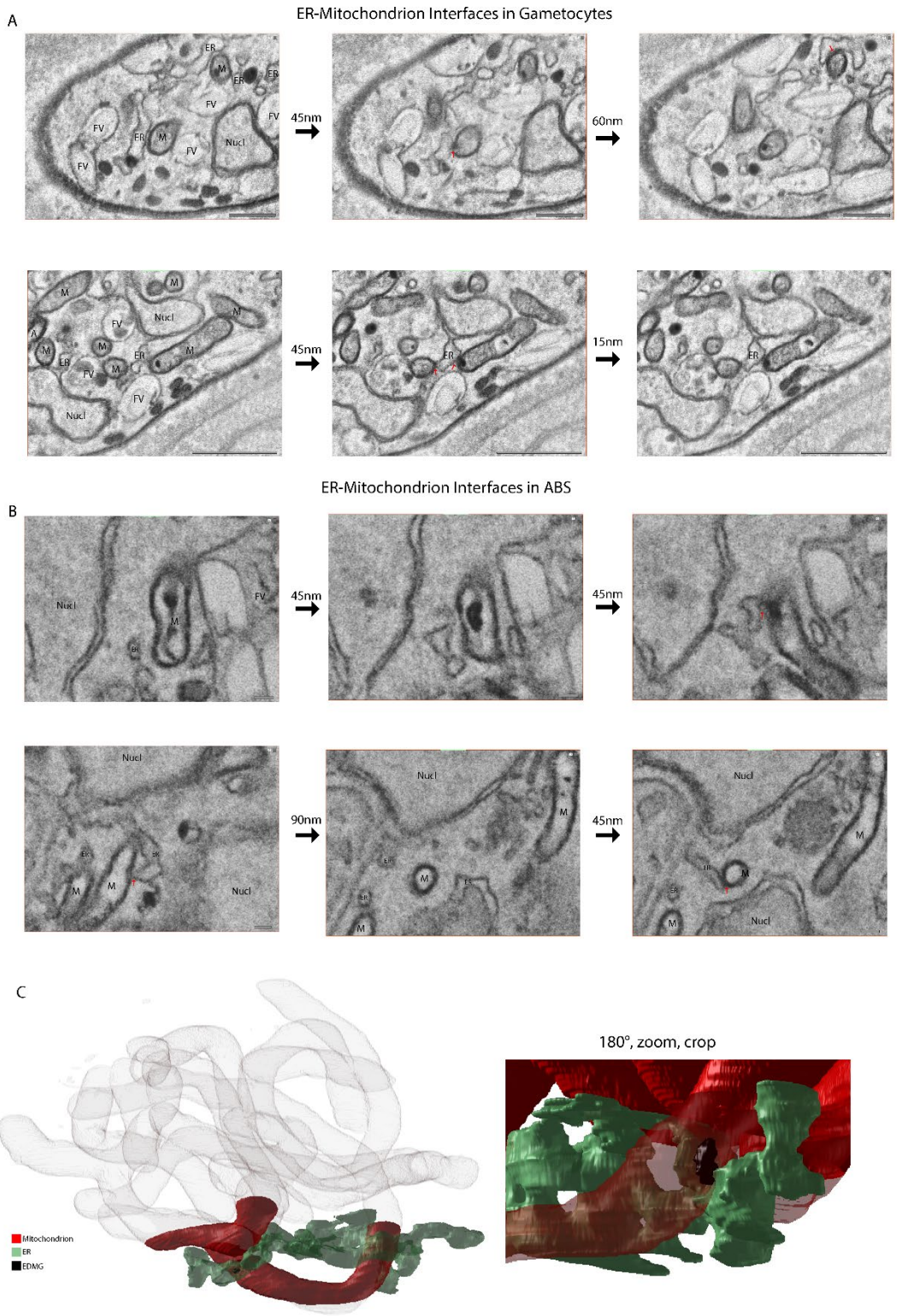

Supp. Figure 11 **ER-mitochondrion interfaces in gametocytes** Series of micrographs showing EDMGs spanning across mitochondrion and ER in gametocytes (**A**) and ABS (**B**). Scale bar A = 0.5 µm in upper panel and 1 µm in lower panel, Scale bar B = 0.1 µm **C** Rendering of EDMG-ER-mitochondrion connection

A

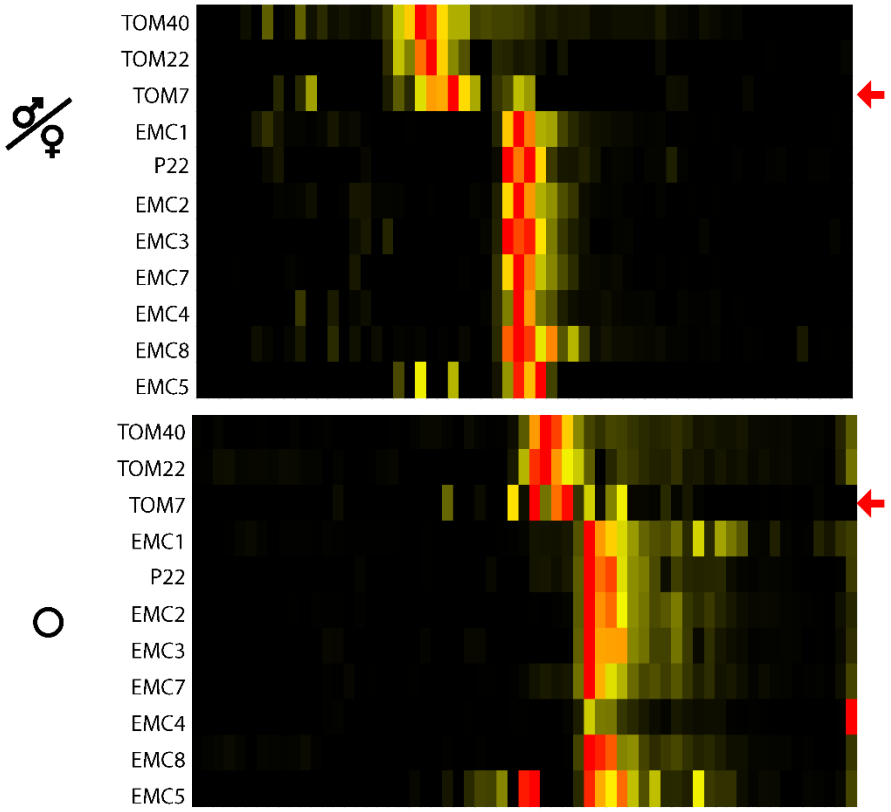

B

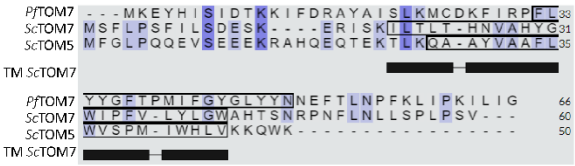

C

	PfTOM7	ScTOM7	ScTOM5
PfTOM7	100.00%	15.79%	12.77%
ScTOM7	15.79%	100.00%	26.09%
ScTOM5	12.77%	26.09%	100.00%

D

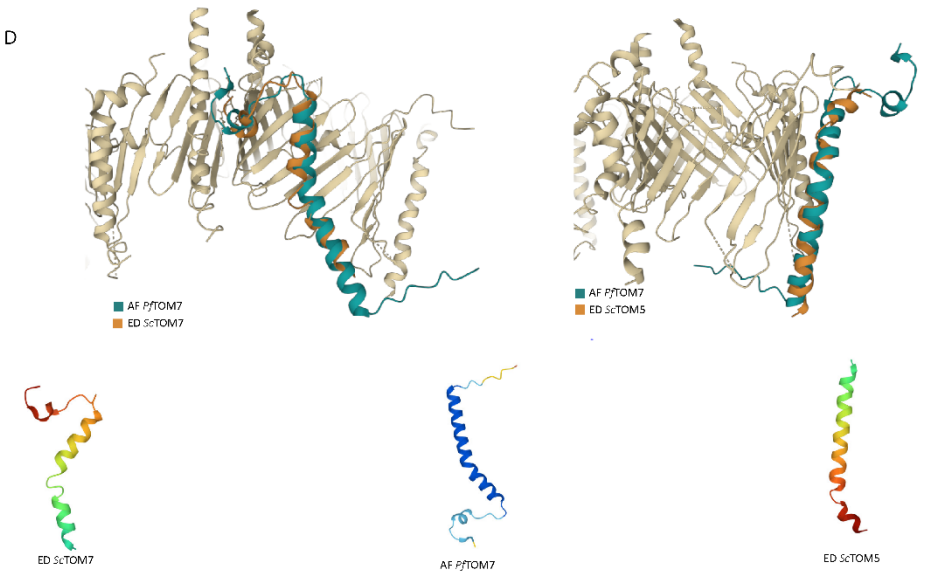

Supp. Figure 12 ***Pf*TOM7 as a putative EMC interactor and MCS facilitator A** Heatmap showing migration of proteins (rows) in native gel electrophoresis (columns). High relative protein abundance is indicated. Appearance in the same column suggests overlapping migrations patterns and putative assignment to a protein interaction. Upper heatmap is derived from a gametocyte sample, lower heatmap is derived from an ABS sample. **B** Multiple sequence alignment of *Pf*TOM7 with *Sc*TOM7 and *Sc*TOM5. Conserved residues have a purple background and residues with light-blue background are conserved in 2/3 sequences. Black boxes show presence of TM domains known from ScTOM7. **C** Sequence similarity matrix shown sequence identity between *Pf*TOM7 with *Sc*TOM7 and *Sc*TOM5. **D** Structural alignment of the alphafold prediction with the experimentally determined structures of *Sc*TOM7 and *Sc*TOM5 in the context of the experimentally determined structure of the TOM complex.